Alma Mater Studiorum · Università di Bologna

Scuola di Scienze
Dipartimento di Fisica e Astronomia
Corso di Laurea Magistrale in Fisica

Test of Lepton Flavour Universality with charm semileptonic decays

Relatore:
Dott. Angelo Carbone

Correlatore:
Dott. Federico Betti

Presentata da:
Alessandra Gioventù

Anno Accademico 2016/2017

Don't Panic

Douglas Adams - "The Hitchicker's Guide to the Galaxy"

Abstract

L'universalità leptonica è una delle simmetrie del Modello Standard (SM). Essa prevede che l'accoppiamento tra i bosoni di gauge e i leptoni delle tre famiglie sia uguale. I recenti risultati sperimentali sulle transizioni $b \to c\ell\nu_\ell$, in particolare gli osservabili R_D e R_{D^*} mostrano una differenza significativa dai valori previsti dal SM, aprendo le porte alla ricerca di nuova fisica anche nei decadimenti di mesoni *charmed*, che a livello di quark corrispondo alla transizione $c \to s\ell\nu_\ell$, dove ℓ può essere un muone o un elettrone. I test dello SM sono studiati attraverso la misura del rapporto $R_{\mu/e}$, definito come $R_{\mu/e} \equiv (d\Gamma^{(\mu)}/dq^2)/(d\Gamma^{(e)}/dq^2)$.

In questa tesi è stato realizzato uno studio preliminare che permette la misura di $R_{\mu/e}$ attraverso la catena di decadimento $D^{*+} \to (D^0 \to K^-\ell^+\nu_\ell)\pi^+$, utilizzando i dati raccolti da LHCb durante il Run-2. Al fine di ottenere le informazioni complete sui prodotti del decadimento $D^0 \to K\ell\nu_\ell$, inclusa la stima del momento del neutrino, è stato implementato un algoritmo di *global fit* (GF). Inoltre, è stata studiata la contaminazione dello spettro di massa invariante del D^{*+}, dovuta a diversi canali di fondo. Per estrarre il numero di eventi di segnale, è stato fatto un fit di chi-quadro sulla massa invariante del D^{*+}, considerando soltanto il fondo combinatorio su un campione di dati, filtrato con dei tagli di PID, utili a ridurre altri fondi.

Contents

Introduction

The lepton flavour universality (LFU) is one of the symmetries of the Standard Model (SM). It predicts equal coupling between gauge bosons and the three lepton families. SM extensions predict additional interactions, implying the possibility of new couplings. The recent experimental results on the $b \to c\ell\nu_\ell$ transitions, in particular the value of the observables R_D and R_{D^*}, show a possible difference with respect to the SM predictions, at the level of about 4.0 standard deviations [1]. These results opened new avenues for new physics (NP) searches also in the charm semileptonic decays. At the quark level charm semileptonic decays correspond to the $c \to s\ell\nu_\ell$ transitions, where ℓ is either a muon or an electron. In particular charm mesons are sensitive to NP. The tests of the SM is carried on through the study of the ratio $R_{\mu/e}$, which is defined as

$$R_{\mu/e} \equiv \frac{d\Gamma^{(\mu)}/dq^2}{d\Gamma^{(e)}/dq^2}. \tag{1}$$

The aim of this thesis is to realise a preliminary study towards the measurement of the observable $R_{\mu/e}$ using the $D^{*+} \to (D^0 \to K^-\ell^+\nu_\ell)\pi^+$ decay. This study is performed with the LHCb data, collected during the Run-2 phase in 2015, corresponding to $0.33\,\text{fb}^{-1}$ of integrated luminosity. The study presented in this thesis is also useful to realize the measurement of $R_{\mu/e}$ as function of q^2, which is the transferred 4-momentum [1]. The decay under study has the peculiarity to be a partially reconstructed decay, as the neutrino is not reconstructed by the LHCb detector.

In order to estimate the momentum of the missing neutrino from the $D^0 \to K\ell\nu_\ell$ decay, a global fit (GF) algorithm is implemented. The GF algorithm consists in a single function which describes the kinematic of the decay, starting from measured quantities. In the detector, the D^{*+} instantly decays into a charged pion and a D^0, which decays after a flight of few centimeters in $K^-\ell^+\nu_\ell$ final state. Taking into account these kinematic properties, 5 contraints are applied in this function: the D^{*+} decay vertex must corresponds to the primary vertex, which is also the decay vertex of the bachelor π; the displaced vertex of the D^0 decay must be formed by the ℓ and K tracks, and the

[1] The transferred 4-momentum of the $i \to f$ transition is defined as $q = p_f - p_i$ where p_i and p_f are the total 4-momenta of the initial and final state, respectively.

invariant mass of the D^0, computed using also the ν momentum, must be equal to its known value. The statistical approach used is the least chi-square method and the final parameters are obtained thanks to a nested minimisation. In particular, these are the momenta of the D^0 decay products $\vec{p}_\nu$, $\vec{p}_\ell$ and $\vec{p}_K$, the coordinates of the π momentum $\vec{p}_\pi$, the position of the secondary decay vertex $\vec{x}_{D^0}$ and finally the third coordinate of the primary vertex $z_{\rm PV}$.

In order to extract the signal yields, a chi-square fit of the D^{*+} invariant mass ($m(D^*)$) is done. In the fit only the combinatorial background component is considered, as the data sample used is filtered with PID requirements useful to reduce other sources of background. However, possible contamination of other sources of backgrounds can be present. For this reason, in addition to the development of the GF algorithm, in this thesis the contamination of the D^{*+} invariant mass spectrum by the different background compontents is evaluated.

This thesis work is organised as follows. In Chapter 1 the theoretical frameworks and an experimental overview of the LFU studies are reported. The LHCb detector is illustrated in Chapter 2. The development of the Global Fit is described in Chapter 3 and how the background is evaluated is described in Chapter 4. Finally the perspectives of this analysis are shown in the Conclusions.

Chapter 1

Theory of leptonic flavour violation in semileptonic decays

The Standard Model of Particle Physics (SM) is the experimentally established theoretical model which describes all the known fundamental interactions, electroweak and strong, with an exception for gravity. The SM describes also the dynamics of sub-atomic particles. These are divided into two families, fermions and bosons, with semi-integer and integer spin respectively. In particular, fermions are divided in leptons (e, μ and τ), which interact only via electroweak force, and quarks (u, d, s, c, b and t), which interact also via the strong one. On the other hand, bosons comprehend the mediators of the electroweak (γ, $W^{\pm}$ and Z) and the strong (eight gluons g) interactions and the Higgs boson H^0, whose role will be described in Sec. 1.1.1.

The SM is described by a Lagrangian density, invariant under non-abelian local gauge transformations. The local gauge symmetry group for the SM is:

$$\mathrm{SU(3)} \times \mathrm{SU(2)} \times \mathrm{U(1)} \tag{1.1}$$

Electroweak interactions are described by the Glashow-Weinberg-Salam model (GWS) [2–4], a non-abelian Yang-Mills quantum field theory, based on the SU(2) × U(1) symmetry group. On the other hand, strong interactions are described by quantum chromodynamics, whose lagrangian is requested to be invariant under SU(3) transformations. These two theories are described in Sec. 1.1 and 1.2.

Even though the SM predictions have never been disproved, there are several observed phenomena not explained. The main ones are the matter-antimatter asymmetry, the nature of dark matter and dark energy, neutrino masses and how gravity can be included in the model. Therefore the SM is an incomplete theory, and new physics phenomena must exist at a certain energy scale. One hypothesis could be considering the SM as the lower-energy limit of a more general theory or as the renormalisable part of an effective field theory valid up to some still undetermined cut-off scale Λ.

In this chapter, after introducing the main features of the SM, the theory of semileptonic decays is described in Sec. 1.3. In particular, the theory of charm mesons decays is described in Sec. 1.4. Finally, in Sec. 1.5 an overview of the latest measurements of semileptonic decays and flavour universality tests are shown.

1.1 The Glashow-Weinberg-Salam model of electroweak interactions

The electroweak part of the lagrangian of the SM, $\mathcal{L}_{GWS}$, can be divided in four different components:

$$\mathcal{L}_{GWS} = \mathcal{L}_B + \mathcal{L}_f + \mathcal{L}_H + \mathcal{L}_Y \tag{1.2}$$

$\mathcal{L}_B$ describes the kinetic term of the four gauge fields B^μ (hypercharge field) and $W^{a\mu}$ (the weak isospin field), with $a = 1, 2, 3$:

$$\mathcal{L}_B = -\frac{1}{4} W^{a\mu\nu} W^a_{\mu\nu} - \frac{1}{4} B^{\mu\nu} B_{\mu\nu}, \tag{1.3}$$

where $B_{\mu\nu}$ and W^{amunu} are the field strength tensors of B^μ and $W^{a\mu}$. $\mathcal{L}_f$ describes the kinetic of the fermions and it has the following form of

$$\mathcal{L}_f = \bar{Q}^j i \not{D}_L Q^j + \bar{u}^j_R i \not{D}_R u^j_R + \bar{d}^j_R i \not{D}_R d^j_R + \bar{L}^j i \not{D}_L L^j + \bar{e}^j_R i \not{D}_R e^j_R, \tag{1.4}$$

where Q^j are the left-handed quark doublets, u_R and d_R are the right-handed quark singlets, L^j are the left-handed lepton doublets, e_R are the electron singlets and a sum over the j generations is assumed.

$$Q^j = \begin{pmatrix} u^j_L \\ d^j_L \end{pmatrix}, \tag{1.5}$$

$$L^j = \begin{pmatrix} {\nu_e}^j \\ e^j_L \end{pmatrix} \tag{1.6}$$

In Eq. (1.4) the covariant derivatives $D_{L\mu}$ and $D_{R\mu}$ are defined as

$$D_{L\mu} = \partial_\mu + igW^a_\mu \frac{\sigma^a}{2} + ig' \frac{Y}{2} B_\mu \tag{1.7}$$

$$D_{R\mu} = \partial_\mu + ig' \frac{Y}{2} B_\mu \tag{1.8}$$

where Y is the hypercharge of the field on which the derivative operates, σ^a are the Pauli matrices, g and g' are the coupling constants. The fields that form the SU(2) doublets have weak isospin $T = 1/2$, with third component $T_3 = \pm 1/2$ for up and down-type fields,

Table 1.1: Value of the quantum numbers for each fermion. The third component of the weak isospin T_3, the hypercharge Y and electromagnetic charge Q are represented.

f	$\mathbf{T_3}$	**Y**	**Q**
u_L	$1/2$	$1/3$	$2/3$
d_L	$-1/2$	$1/3$	$-1/3$
u_R	0	$4/3$	$2/3$
d_R	0	$-2/3$	$-1/3$
ν_L	$1/2$	-1	0
e_L	$-1/2$	-1	-1
e_R	0	-2	-1

respectively. The right-handed fermion fields, which are SU(2) singlets, have $T = 0$.

The electromagnetic charge of a field Q can be defined as a function of the hypercharge Y and the third coordinate of the weak isospin T_3:

$$Q = \frac{Y}{2} + T_3 \tag{1.9}$$

From this definition it is possible to obtain the values of the hypercharges of all fermionic doublets and singlets according to their electromagnetic charge.

The third term of the electroweak lagrangian is the Higgs term $\mathcal{L}_H$. It describes the Higgs field and its coupling with the bosons.

$$\begin{aligned} \mathcal{L}_H &= (D^\mu \phi^\dagger)(D_\mu \phi) - V(\phi^\dagger \phi) \\ &= (D^\mu \phi^\dagger)(D_\mu \phi) - \left(-\mu^2 \phi^\dagger \phi + \frac{\lambda^2}{2} (\phi^\dagger \phi)^2 \right), \end{aligned} \tag{1.10}$$

where λ and μ are positive parameters and ϕ is the Higgs doublet. ϕ follows SU(2) symmetry and it has hypercharge 1

$$\phi = \begin{pmatrix} \phi^+ \\ \phi^0 \end{pmatrix}. \tag{1.11}$$

ϕ^+ has electromagnetic positive charge and it is a SU(2) doublet with hypercharge 1, while ϕ^0 is neutral charged. It follows that the covariant derivative operating on ϕ^+ is the left-handed one

$$D_\mu = \partial_\mu + igW_\mu^a \frac{\sigma^a}{2} + ig' \frac{Y}{2} B_\mu. \tag{1.12}$$

Finally, the last term of the GWS model lagrangian, $\mathcal{L}_\mathbf{Y}$, concerns the Yukawa interaction between the fermion fields and ϕ. Assuming a sum over i and j, it has the

following form

$$\mathcal{L}_Y = -\lambda_d^{ij}\overline{Q}^i\phi {d_R}^j - \lambda_u^i\overline{Q}^j(i\sigma^2\phi)u_R^j - g_e^i\overline{L}^i e_R^i + \text{h.c.}\,, \tag{1.13}$$

where $\lambda_{d,u}^{ij}$ are general complex matrices and g_e^i are coupling constants.

1.1.1 The Brout-Englert-Higgs mechanism

Particle masses are generated through the spontaneous symmetry breaking of the local gauge symmetry $\mathrm{SU}(2)_L \times \mathrm{U}(1)_Y$ [5,6]. In fact, it is possible to reduce the four degrees of freedom of ϕ to one, through the SU(2) gauge invariance. The Higgs doublet can be written in the unitarity gauge and then expanded around its own vacuum expectation value (VEV). In particular, the Higgs potential $V(\phi^\dagger\phi)$ has a minimum when

$$\phi^\dagger\phi = \frac{\mu^2}{\lambda^2} \equiv \frac{v^2}{2} \tag{1.14}$$

where $v/\sqrt{2}$ is the VEV of ϕ and it is about $v \simeq 246\,\text{GeV}$. Then ϕ becomes

$$\phi(x) = \frac{1}{\sqrt{2}}\begin{pmatrix} 0 \\ v + H(x) \end{pmatrix}, \tag{1.15}$$

where $H(x)$ is the invariant Higgs field, which is scalar and real. At this point, the lagrangian is no longer gauge invariant.

Due to the $\mathrm{SU}(2)_L \times \mathrm{U}(1)_Y$ group's degrees of freedom, after the breaking there will be one massless and three Goldstone bosons. This is a consequence of the Goldstone theorem, which states that massless scalars occur whenever a continuous symmetry of a physical system is spontaneously broken. In particular the gauge fields are redefined as

$$W_\mu^\pm = \frac{W_\mu^1 \mp iW_\mu^2}{\sqrt{2}}\,, \tag{1.16}$$

$$Z_\mu = W_\mu^3 \cos\theta_\text{W} - B_\mu \sin\theta_\text{W}\,, \tag{1.17}$$

$$A_\mu = W_\mu^3 \sin\theta_\text{W} + B_\mu \cos\theta_\text{W}\,, \tag{1.18}$$

where θ_W is the Weinberg angle, with $\sin^2\theta_\text{W} \simeq 0.23$. At this point the Higgs term of the lagrangian (1.10), substituting Equation (1.15) becomes:

$$\mathcal{L}_H = -\frac{1}{8}g^2v^2(W^{+\mu}W_\mu^+ + W^{-\mu}W_\mu^-) - \frac{1}{8}v^2(g^2+g'^2)Z^\mu Z_\mu - \frac{1}{2}\lambda^2v^2H^2 \tag{1.19}$$

It follows that the masses of the gauge bosons are

$$M_H = \lambda v\,, \tag{1.20}$$

$$M_W = \frac{1}{2} g v\,, \tag{1.21}$$

$$M_Z = \frac{1}{2} v \sqrt{g^2 + g'^2}\,, \tag{1.22}$$

$$M_\gamma = 0 \tag{1.23}$$

After the SSB the lagrangian defining Yukawa couplings of Equation (1.13) changes to

$$\mathcal{L}_Y = -\frac{v}{\sqrt{2}} \lambda_d^{ij} \overline{d}_L^i d_R^j - \frac{v}{\sqrt{2}} \lambda_u^{ij} \overline{u}_L^i u_R^j - \frac{v}{\sqrt{2}} g_e^i \overline{e}_L^i e_R^i + \text{h.c.} \tag{1.24}$$

As a consequence, the mass of the e^i is equal to

$$M_{e^i} = \frac{v}{\sqrt{2}} g_e^i. \tag{1.25}$$

The mass of the lepton (electron, muon or tauon) is proportional to the coupling between the lepton and the Higgs Boson, while the neutrino, which does not appear, remains massless.

1.1.2 The Cabibbo-Kobaiashi-Maskawa matrix

Quarks masses are generated differently than leptons. The two eigenstates u^i and d^i do not correspond to physical particles. In order to obtain the mass values observed experimentally, mass eigenstates have to be introduced. This is why in Eq. (1.24) the $\lambda_{u,d}$ matrices have been introduced. The mass term for physical quarks are obtained by diagonalising $\lambda_{u,d}$, introducing unitary matrices $U_{u,d}$ and $W_{u,d}$ [7, 8]:

$$\begin{aligned} \lambda_{u,d} \lambda_{u,d}^\dagger &= U_{u,d} D_{u,d}^2 U_{u,d}^\dagger, \\ \lambda_{u,d}^\dagger \lambda_{u,d} &= W_{u,d} D_{u,d}^2 W_{u,d}^\dagger, \end{aligned} \tag{1.26}$$

where $D_{u,d}$ are diagonal matrices. This leads to

$$\lambda_{u,d} = U_{u,d} D_{u,d} W_{u,d}^\dagger. \tag{1.27}$$

At this point, the physical quark fields can be defined as

$$\begin{aligned} u_L^i &= U_u^{ij} u_L^{j,phys}, \\ u_R^i &= W_u^{ij} u_R^{j,phys}, \\ d_L^i &= U_d^{ij} d_L^{j,phys}, \\ d_R^i &= W_d^{ij} d_R^{j,phys} \end{aligned} \tag{1.28}$$

Together with Eq. (1.27), it allows to get in the Yukawa lagrangian $\mathcal{L}_Y$ the terms:

$$-\frac{v}{\sqrt{2}} D_u^{ii} \bar{u}^{i,phys} u^{i,phys} - \frac{v}{\sqrt{2}} D_d^{ii} \bar{d}^{i,phys} d^{i,phys} \tag{1.29}$$

The quark masses are defined as

$$m_{u,d}^i = \frac{v}{\sqrt{2}} D_u^{ii} \tag{1.30}$$

Moreover, the replacement of weak eigenstates quark fields with mass eigenstates has another important effect. It is possible to demonstrate that in the GWS lagrangian the following terms are present

$$-\frac{g}{\sqrt{2}} (J^{+\mu} W_\mu^+ + J^{-\mu} W_\mu^-) - \frac{g}{\cos\theta_{\mathrm{W}}} J^{N\mu} Z_\mu \tag{1.31}$$

where $J^{\pm\mu}$ and $J^{N\mu}$ are the charged and neutral currents, defined as

$$J^{+\mu} = \overline{\nu}_L^a \gamma^\mu e_L^a + \bar{u}_L^a \gamma^\mu d_L^a, \tag{1.32}$$

$$J^{-\mu} = \mathrm{h.c.}(J^{+\mu}), \tag{1.33}$$

$$J^{N\mu} = \sum_{a,f} \bar{f}^a \frac{\gamma^\mu}{2} \left[T_3 - (T_3 - 2\sin^2\theta_{\mathrm{W}} Q)\gamma^5 \right] f^a, \tag{1.34}$$

where f^a stands for a generic fermion (neutrino, electron or quark) of the a-th generation, T_3 its weak isospin and Q its electromagnetic charge.

Using the mass eigenstates, the terms involving quarks in the charged current of Eq. (1.32) can be written in this form:

$$J_{quarks}^{+\mu} = \bar{u}_L^{i,phys} (U_u^\dagger U_d)^{ij} \gamma^\mu d_L^{j,phys} \tag{1.35}$$

The matrix $U_u^\dagger U_d \equiv V_{CKM}$ is the Cabibbo-Kobayashi-Maskawa matrix (CKM). The charged-current interaction lagrangian for quarks can now be written in this way:

$$\mathcal{L}_{cc,quarks} = -\frac{g}{\sqrt{2}} \begin{pmatrix} \bar{u}_L & \bar{c}_L & \bar{t}_L \end{pmatrix} \begin{pmatrix} V_{ud} & V_{us} & V_{ub} \\ V_{cd} & V_{cs} & V_{cb} \\ V_{td} & V_{ts} & V_{tb} \end{pmatrix} \gamma^\mu \begin{pmatrix} d_L \\ s_L \\ b_L \end{pmatrix} W_\mu^+ + \mathrm{h.c.}, \tag{1.36}$$

where the spinors represent the physical quark fields. As a consequence, the $W^{\pm}$ bosons mediate interactions between up-type and down-type quarks also between different families, so the quark flavour can change in weak interactions. Every element of the CKM matrix describes the coupling strength between two different quarks. For example $|V_{tb}| \simeq 1$ and $|V_{ub}| \simeq 0.004$, means that the coupling between t and b is very strong compared to the one between u and b.

The CKM matrix can be parameterized by three mixing angles θ_{ij} and a *CP*-violating phase δ. Defining $s_{ij} = \sin\theta_{ij}$ and $c_{ij} = \cos\theta_{ij}$, the CKM matrix becomes

$$V_{CKM} = \begin{pmatrix} c_{12}c_{13} & s_{12}c_{13} & s_{13}e^{-i\delta} \\ -s_{12}c_{23} - c_{12}s_{23}s_{13}e^{i\delta} & c_{12}c_{23} - s_{12}s_{23}s_{13}e^{i\delta} & s_{23}c_{13} \\ s_{12}s_{23} - c_{12}s_{23}s_{13}e^{i\delta} & -c_{12}s_{23} - s_{12}c_{23}s_{13}e^{i\delta} & c_{23}c_{13} \end{pmatrix} + \mathcal{O}(\lambda^4), \quad (1.37)$$

Experimentally it is known that $s_{13} \ll s_{23} \ll s_{12} \ll 1$. For this reason, the Wolfenstein parametrisation, which takes into account the hierarchy of the matrix elements, can be used. Thus, the CKM matrix becomes

$$V_{CKM} = \begin{pmatrix} 1 - \lambda^2/2 & \lambda & A\lambda^3(\rho - i\eta) \\ -\lambda & 1 - \lambda^2/2 & A\lambda^2 \\ A\lambda^3(1 - \rho - i\eta) & -A\lambda^2 & 1 \end{pmatrix} + \mathcal{O}(\lambda^4) \quad (1.38)$$

where

$$\begin{aligned} s_{12} = \lambda &= \frac{|V_{us}|}{\sqrt{|V_{ud}|^2 + |V_{us}|^2}}, \\ s_{23} = A\lambda^2 &= \lambda \left| \frac{V_{cb}}{V_{us}} \right|, \\ s_{13}e^{i\delta} = V_{ub}^* &= A\lambda^3(\rho + i\eta). \end{aligned} \quad (1.39)$$

It is possible to evaluate the CKM matrix elements, through different tree-level processes. For example V_{ud} is obtained studying beta decays while V_{tb} is known from the branching ratio of the $t \to Wb$ transition. According to the latest measurements, the CKM matrix has the values represented in Table 1.2 [9].

Finally, the CKM matrix shows another important feature of the electroweak theory: the non existence of Flavour-Changing Neutral Currents (FCNC) at tree-level in the SM [7, 10]. In fact, after substituting the mass eigenstates in Eq. (1.34) it is clear that a fermion only interact with its antiparticle or an identical fermion in neutral-current interactions. This is possible thanks to the unitarity of $U_{u,d}$ and $W_{u,d}$.

V_{CKM} ELEMENT	VALUE
V_{ud}	(0.97431 ± 0.00015)
V_{us}	(0.22512 ± 0.00067)
V_{ub}	$(0.00365 \pm 0.00012)e^{i(-65.88\pm1.88)^\circ}$
V_{cd}	$(-0.22497 \pm 0.00067)e^{i(0.0352\pm0.0010)^\circ}$
V_{cs}	$(0.97344 \pm 0.00015)e^{i(-0.001877\pm0.000055)^\circ}$
V_{cb}	(0.04255 ± 0.00069)
V_{td}	$(0.00869 \pm 0.00014)e^{i(-22.00\pm0.73)^\circ}$
V_{ts}	$(-0.04156 \pm 0.00056)e^{i(1.040\pm0.035)^\circ}$
V_{tb}	(0.999097 ± 0.000024)

Table 1.2: Values of the CKM matrix elements according to the latest measurements [9].

1.2 Quantum chromodynamics

Quantum Chromodynamics (QCD) is the theory which explains the strong interactions between quarks and gluons. QCD is a Yang-Mills [11] non-abelian quantum field theory based on the exact and unbroken colour-SU(3) local gauge symmetry. The QCD lagrangian is:

$$\mathcal{L}_{QCD} = \sum_f \overline{\psi}_f \left(i\gamma^\mu \partial_\mu - g_s \gamma^\mu \frac{\lambda^C}{2} A^C_\mu - m_f \right) \psi_f - \frac{1}{4} A^{C\mu\nu} A^C_{\mu\nu} \tag{1.40}$$

where ψ_f is a triplet in the SU(3) space of quark spinors of flavour f and mass m_f, g_s is the strong coupling constant, A^C_μ are the massless gluon fields (C = 1, ..., 8), $A^{C\mu\nu}$ are the gluon field strenght tensors and λ^C are the eight Gell-Mann matrices, generators of the SU(3) group. The strong coupling constant has a dependence on the exchanged momentum q^2:

$$g_s = \frac{8\pi^2}{(11 - \frac{2}{3}n_f)\log(q/\Lambda_{\mathrm{QCD}})}, \tag{1.41}$$

where n_f is the number of flavours and Λ_{QCD} is the energy scale of strong interactions, which is about 200 MeV experimentally. The magnitude of the coupling constant decreases with increasing q^2 or with decreasing distances. As a consequence, quarks and gluons behave as quasi-free particles at high energies, when $q \gg \Lambda_{\mathrm{QCD}}$, and at low energies, $q \ll \Lambda_{\mathrm{QCD}}$, the coupling constant becomes very high. This means that only at high energies quark-gluon interactions can be treated perturbatively, expanding in series of $\alpha_s = g_s/4\pi$.

1.3 Theory of semileptonic decays

The amplitude of the semileptonic decay of a meson M_{Qq} into a state containing a meson $M_{q'q}$ can be written as a term proportional to the product of a leptonic current L_μ (1.44) and a hadronic current H_μ (1.45). In particular, if the exchanged four-momentum q is much smaller than the mass M_W of the $W^\pm$ boson, the amplitude can be written in the following way:

$$\mathcal{M} = -i\frac{G_F}{\sqrt{2}} V_{Qq'} L^\mu H_\mu \tag{1.42}$$

where p and p' are the respective momenta of M_{Qq} and $M_{q'q}$, $q = p - p'$ and G_F is the Fermi constant, defined as

$$G_F = \frac{g^2\sqrt{2}}{8M_W^2} = 1.16638 \times 10^{-5}\,\mathrm{GeV}^{-2}. \tag{1.43}$$

The leptonic and hadronic currents are respectively given by

$$L^\mu = \bar{\ell}\gamma^\mu(1-\gamma_5)\nu_\ell, \tag{1.44}$$

$$H_\mu = \langle M_{q'q}(p')|j_\mu^H|M_{Qq}(p)\rangle, \tag{1.45}$$

where j_μ^H, a four-current, can be expressed in term of Lorentz-invariant quantities, combinations of $(p_\mu + p'_\mu)$, q_μ and q^2.

Due to the fact that the two mesons interact also strongly, the hadronic current will contain some terms that parameterise the non-perturbative behaviour of the QCD. These terms are called form factors f. The form factors depend on the given initial and final state and they are measurable experimentally. Several methods exist to calculate these form factors, one of them is the Heavy Quark Effective Theory [12].

1.3.1 The Heavy Quark Effective Theory

The Heavy Quark Effective Theory (HQET) is an effective theory which aims to describe the strong interaction between a single heavy quark (b or c) and a light one [13]. The approach is similar to Fermi's effective theory where the weak interactions were approximated by point-like couplings, governed by a dimensionful coupling constant G_F. Only at energies much larger than the masses of hadrons the effects of the intermediate vector bosons, W and Z, can be resolved. A diagram of the semileptonic decay $Q \to q'\ell\nu_\ell$ studied using HQEFT is represented in Fig. 1.1.

The starting point of the HQET is the approximation of the mass of the heavy quark m_Q as infinite. In this way, the heavy quark acts like a stationary source of colour charge. The effective lagrangian is constructed by expanding the QCD lagrangian $\mathcal{L}_{QCD}$ in a

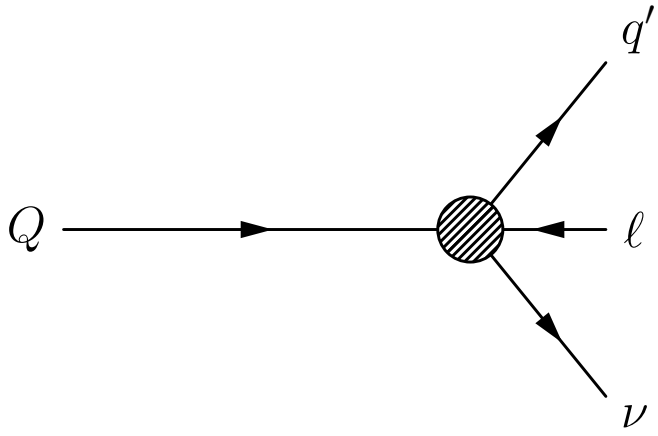

Figure 1.1: Diagram of a semileptonic decay studied by the effective theory, where Q is the heavy quark, q' the lighter one.

power seres of $1/m_Q$ and neglecting higher-order terms, as far as $m_Q \gg \Lambda_{\rm QCD}$. HQET is particularly useful to calculate the form factors of decays involving charm mesons transitions, in particular $c \to s$ one. In fact, the velocity transferred between the two quarks is small, leaving the colour source stationary to a good approximation.

Another important feature, shared by all effective theories, is the definition of the Wilson coefficient $\mathcal{C}$, which give information on the coupling constants.

1.4 The $c \to s\ell\nu_\ell$ transitions

The semileptonic decays of charm mesons, which at the quark level correspond to $c \to s\ell\nu_\ell$ transitions, might offer important test of the SM predictions. In particular, they can be used as probes of the lepton flavour universality (LFU), since they are $|\Delta F| = 1$ processes, where F is the flavour. One of the observable used to test LFU studying heavy mesons decays is the ratio between the decay rates of two decay channels with different leptonic daughters. For instance, the decays studied in this thesis are $D^0 \to K\ell\nu_\ell$ where the lepton is either a muon or an electron and the ratio of the two decay rates $R_{\mu/e}$ is defined as

$$R_{\mu/e}(q^2) \equiv \frac{d\Gamma^{(\mu)}/dq^2}{d\Gamma^{(e)}/dq^2}. \tag{1.46}$$

In the past few years, a significant effort has been made in both theoretical and experimental research of these transitions. On the theoretical side, for example, the shapes of the semileptonic form factors $f_{+,0}(q^2)$ for the process $D \to K\ell\nu$ over the whole physical q^2 region were recently calculated in the lattice QCD [14].

1.4.1 Theoretical predictions for $R_{\mu/e}$

Within the SM, the theoretical predictions for $c \to s\ell\nu_\ell$ decays can be compared to the measured values of the total or differential branching fractions in order to extract the $|V_{cs}|$ element of CKM matrix. The constrains on the effects of the new physics (NP) in a given process can be derived after fixing the value of the CKM matrix element from some independent source.

Following [15], for the $c \to s\ell\nu_\ell$ transitions, the effective Lagrangian can be written as

$$\mathcal{L}_{eff} = -\frac{4G_F}{\sqrt{2}} V_{cs} \sum_{\ell=e,\mu,\tau} \sum_i \mathcal{C}_i^{(\ell)} \mathcal{O}_i^{(\ell)} + \text{h.c.}. \tag{1.47}$$

where $\mathcal{C}_i$ are the Wilson coefficient, which are defined as $\mathcal{C}_i(\Lambda) = (F_i L_i)/\Lambda^2$, with F_i functions of the NP flavour couplings, L_i the loop factors present in models without tree-level FCNC and Λ the NP energy scale. When the coefficient $\mathcal{C}_{SM}^{(\ell)} = 1$, the four-fermion operator $\mathcal{O}^{(\ell)}$ is in the form

$$\mathcal{O}_{SM}^{(\ell)} = \big(\bar{s}\gamma_\mu P_L c\big)\big(\bar{\nu}_\ell \gamma^\mu P_L \ell\big) \tag{1.48}$$

where $P_{L,R} = \frac{(1 \mp \gamma_5)}{2}$.The interesting non-standard effective operators, which involve (pseudo)scalar quark and lepton densities and keep only the left-handed neutrinos, have the form

$$\mathcal{O}_{L(R)}^{(\ell)} = \big(\bar{s} P_{L(R)} c\big)\big(\bar{\nu}_\ell P_R \ell\big). \tag{1.49}$$

By integrating out the beyond SM scalar boson at the tree level these operators may be induced. The extension of the SM called two-Higgs doublet model (THDM) is one of the theories which can provide such scalar boson. The type-II THDM is one of the most studied models. In this $\mathcal{C}_{R(L)}^{(\ell)}$ can be expressed as the combination of two real parameters, the mass of the charged scalar H^+ and $\tan\beta$, *i.e.* the ratio of the vacuum expectation values of the doublets. In general, $\mathcal{C}_{R(L)}^{(\ell)}$ can be considered complex and they depend of the flavour of the charged lepton. The combination of the Wilson coefficients $\mathcal{C}_S^{(\ell)} = \mathcal{C}_R^{(\ell)} + \mathcal{C}_L^{(\ell)}$ affects the semileptonic $D \to K\ell\nu$ decay rate.

The hadronic matrix element of the vector current for the $D(k) \to K(k')\ell\nu_\ell$ decay is

parametrized by form factors $f_{+,0}(q^2)$ as

$$\langle K(k')|\bar{s}\gamma_\mu c|D(k)\rangle = f_+(q^2)\left((k+k')_\mu - \frac{m_D^2 - m_K^2}{q^2}q_\mu\right) + f_0(q^2)\frac{m_D^2 - m_K^2}{q^2}q_\mu\,, \quad (1.50)$$

with the usual kinematic constraint $f_+(0) = f_0(0)$. The matrix element of the scalar density is related to the form factor $f_0(q^2)$ through the partially conserved vector current identity, $\partial_\mu(\bar{s}\gamma_\mu c) = i\,(m_s - m_c)(\bar{s}c)$, and it becomes

$$\langle K|\bar{s}c|D\rangle = \frac{m_D^2 - m_K^2}{m_s - m_c}f_0(q^2). \quad (1.51)$$

The differential decay rate of the process $D \to K\ell\nu_\ell$ is given by the formula

$$\frac{d\Gamma^{(\ell)}}{dq^2} = \frac{G_F^2|V_{cs}|^2|\mathbf{q}|q^2}{96\pi^3 m_D^2}\left(1 - \frac{m_\ell^2}{q^2}\right)^2\left[|h_0(q^2)|^2\left(1 + \frac{m_\ell^2}{2q^2}\right) + \frac{3m_\ell^2}{2q^2}|h_t(q^2)|^2\right], \quad (1.52)$$

where $|\mathbf{q}|$ is the magnitude of the transferred three-momentum in the rest frame of the D meson, defined as

$$\begin{aligned} |\mathbf{q}| &= \sqrt{\lambda(m_D^2, m_K^2, q^2)}/2m_D \\ \lambda(x,y,z) &= x^2 + y^2 + z^2 - 2(xy + xz + yz) \end{aligned} \quad (1.53)$$

and $h_{0,t}$ are the non-vanishing hadronic helicity amplitudes for the transition $D \to K\ell\nu$. They are defined as $\tilde{\epsilon}_{0,t}^{\mu *}\langle K|J_\mu|D\rangle$ and are given explicitly by:

$$\begin{aligned} h_0(q^2) &= \frac{\sqrt{\lambda(m_D^2, m_K^2, q^2)}}{\sqrt{q^2}}f_+(q^2), \\ h_t(q^2) &= \left(1 + g_S^{(\ell)}\frac{q^2}{m_\ell(m_s - m_c)}\right)\frac{m_D^2 - m_K^2}{\sqrt{q^2}}f_0(q^2) \end{aligned} \quad (1.54)$$

The functional dependence on the q^2 of the form factors $f_{+,0}$ was recently calculated in lattice QCD by the HPQCD collaboration in Ref. [14]. Using their results and the measured branching fractions the constraint on the Wilson coefficients $\mathcal{C}_S^{(\mu)} \equiv \mathcal{C}_R^{(\mu)} + \mathcal{C}_L^{(\mu)}$ are derived. In the case of electron, the 95% C.L. interval reads: $|\mathcal{C}_S^{(e)}| < 0.2$. The CLEO collaboration measured [16] the differential decay rate for the process with electrons in the final state. The corresponding constraint is not significantly more stringent than the one obtained from the full branching ratio. In Fig. 1.2 the allowed range for the ratio $R_{\mu/e}(q^2)$ assuming $\mathcal{C}_S^{(e)} = 0$, derived by [15] is represented.

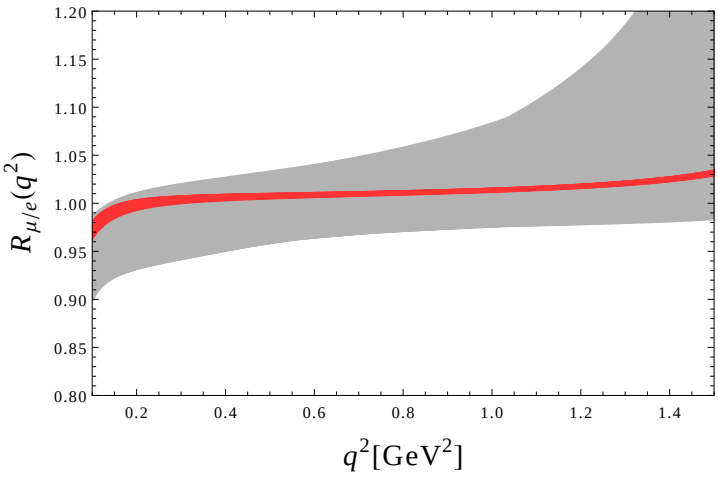

Figure 1.2: The ratio $R_{\mu/e}(q^2) \equiv \frac{d\Gamma^{(\mu)}}{dq^2} / \frac{d\Gamma^{(e)}}{dq^2}$ in function of the q^2, assuming $\mathcal{C}_S^{(e)} = 0$, is represented. In grey the SM predictions and in red the allowed deviations are shown [15].

1.5 Experimental overview of LFU in semileptonic decays

In the past few years many measurements of LFU in semileptonic have been performed. In particular some tension from the SM have been observed in $b \to s\ell^-\ell^+$ and $b \to c\ell\nu_\ell$ transitions. In this section, an overview of these important results and the current experimental status are given.

1.5.1 LFU probes studying R_K

R_K is the measurement of the ratio of the differential branching fractions of $B^+ \to K^+\ell^+\ell^-$ decays in a given range of q^2:

$$R_K = \frac{\int_{q^2_{min}}^{q^2_{max}} \frac{d\Gamma(B^+ \to K^+\mu^+\mu^-)}{dq^2} dq^2}{\int_{q^2_{min}}^{q^2_{max}} \frac{d\Gamma(B^+ \to K^+e^+e^-)}{dq^2} dq^2} \tag{1.55}$$

The Standard Model prediction of R_K is 1.00030 with an uncertainty of $\Delta R_K = +3\%$ arising from QED corrections [17]. In order to minimise uncertainties, the LHCb Collaboration has measured R_K [18] in the theoretically preferred range $1 < q^2 < 6\,\text{GeV}/c^2$ as a double ratio with respect to the normalisation channel $B^+ \to K^+ J/\psi$, where the J/ψ decays either to a di-muon or di-electron final state.

$$R_K = \frac{N_{K^+\mu^+\mu^-} N_{J/\psi(e^+e^-)K^+}}{N_{K^+e^+e^-} N_{J/\psi(\mu^+\mu^-)K^+}} \frac{\epsilon_{K^+e^+e^-}}{\epsilon_{K^+\mu^+\mu^-}} \frac{\epsilon_{J/\psi(e^+e^-)K^+}}{\epsilon_{J/\psi(\mu^+\mu^-)K^+}} \tag{1.56}$$

The efficiencies comprise effects from each step of the analysis. Overall, the efficiency to reconstruct, select and identify a muon is two times higher than for an electron. The R_K measurement is performed on the 3 fb^{-1} dataset recorded in 2011 (2012) at centre-of-mass energies of $\sqrt{s} = 7(8)$ TeV. The results yield $R_K = 0.745^{+0.090}_{-0.074} \pm 0.036$, which corresponds to a 2.6σ deviation from the Standard Model prediction.

The Belle Collaboration has published a measurement of R_K in the full q^2 range, $R_K^{\text{Belle}} = 1.03 \pm 0.19 \pm 0.06$ [19], whereas the BaBar Collaboration has studied the low and high q^2 regions, measuring $R_K = 0.74^{+0.40}_{-0.31} \pm 0.06$ and $R_K = 1.43^{+0.65}_{-0.44} \pm 0.12$ [20], respectively. The measurements from the B-factories are compatible with the Standard Model prediction within less than one standard deviation.

1.5.2 Test of LFU studying R_D and R_{D^*}

Beyond the Standard Model physics could appear not only in loops to which R_K is sensitive but also at tree level. The latter has been studied at LHCb with $\overline{B}^0 \to D^{*+}\tau^-\overline{\nu}_\tau$ transitions [21] through the branching fraction

$$R_{D^*} = \frac{\mathcal{B}(\overline{B}^0 \to D^{*+}\tau^-\overline{\nu}_\tau)}{\mathcal{B}(\overline{B}^0 \to D^{*+}\mu^-\overline{\nu}_\mu)} \tag{1.57}$$

The BaBar Collaboration had previously observed deviations from the Standard Model prediction [22] in R_{D^*} and the analogously defined R_D corresponding to a combined significance of 3.4σ [23], where neutral as well as charged B meson decays were studied. In addition to muons, the BaBar measurement includes electrons in the final state of the signal and normalisation channels.

The LHCb analysis on the dataset of 3 fb^{-1} of 2011 and 2012, reconstruct the $\overline{B}^0 \to D^{*+}\tau^-\overline{\nu}_\tau$ decay with $\tau^- \to \mu^-\overline{\nu}_\mu\nu_\tau$. The LHCb result is $R_{D^*} = 0.336 \pm 0.027 \pm 0.030$, and it corresponds to a 2.1σ deviation from the Standard Model prediction. The result of the combination of various R_D and R_{D^*} exhibits a tension of 3.9σ between the combined average and the Standard Model prediction.

The latest LHCb analysis [24, 25] measure R_{D^*} using three-prong tauon decays, $B^0 \to D^{*-}\pi^+\pi^-\pi^+$, as a renormalisation channel in order to reduce experimental systematic uncertainties, due to the two neutrinos in the final state of the $\tau^- \to \mu^-\overline{\nu}_\mu\nu_\tau$ decay. In [25] a value of $R_{D^*} = 0.286 \pm 0.019 \pm 0.025 \pm 0.021$ is obtained.

The current global average is $R_{D^*} = 0.304 \pm 0.013 \pm 0.007$ [1] and the combination of the measurements of R_D vs R_{D^*} is represented in Fig. 1.3.

1.5.3 $R_{\mu/e}$ from $c \to d\ell\nu_\ell$ transitions

The BESIII collaboration at the e^+e^- collider BEPCII published its latest results on LFU in [26] early this year. In particular $D^{0(+)} \to \pi^{-(0)}\ell^+\nu_\ell$ transitions have been

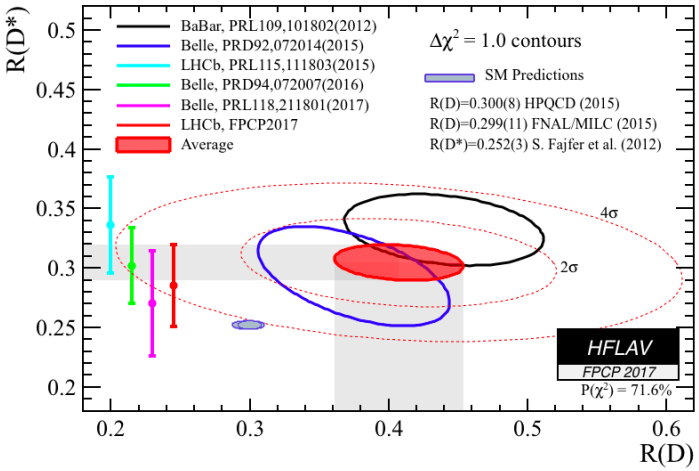

Figure 1.3: Combination of the measurements of R_D and R_{D^*} [1].

studied, and the ratio is calculated as

$$R^0_{\mu/e} = \frac{\mathcal{B}(D^0 \to \pi^- \mu^+ \nu_\mu)}{\mathcal{B}(D^0 \to \pi^- e^+ \nu_e)}, \tag{1.58}$$

$$R^+_{\mu/e} = \frac{\mathcal{B}(D^+ \to \pi^0 \mu^+ \nu_\mu)}{\mathcal{B}(D^+ \to \pi^0 e^+ \nu_e)}. \tag{1.59}$$

The branching fractions for $D^{0(+)} \to \pi^{-(0)} \mu^+ \nu_\mu$ have been calculated using a data sample corresponding to an integrated luminosity of 2.93 fb^{-1}, taken at centre-of-mass energy of 3.773 GeV. The obtained values of the branching ratios $\mathcal{B}$ are $\mathcal{B}(D^0 \to \pi^- \mu^+ \nu_\mu) = (0.267 \pm 0.007\,_{\text{(stat)}} \pm 0.007\,_{\text{(syst)}})\%$ and $\mathcal{B}(D^+ \to \pi^0 \mu^+ \nu_\mu) = (0.342 \pm 0.011\,_{\text{(stat)}} \pm 0.010\,_{\text{(syst)}})\%$. The two ratios have been calculated using previous BESIII measurements, obtaining the values

$$R^0_{\mu/e} = 0.905 \pm 0.027\,_{\text{(stat)}} \pm 0.023\,_{\text{(syst)}}, \tag{1.60}$$

$$R^+_{\mu/e} = 0.942 \pm 0.037\,_{\text{(stat)}} \pm 0.027\,_{\text{(syst)}}, \tag{1.61}$$

which are compatible with the theoretical prediction of lepton universality within 1.9σ and 0.6σ, respectively.

1.5.4 Test of LFU in $W \to \ell\nu_\ell$ decays

A further test of lepton flavour universality on tree level processes is performed with $W \to \ell\nu_\ell$ decays utilised for a measurement of the forward production cross-section on the 2 fb^{-1} dataset recorded in 2012 at $\sqrt{s} = 8$ TeV. The combination of the two separate analyses of $W \to e\nu_e$ [27] and $W \to \mu\nu_\mu$ [28] allow to extract the ratio of branching fractions

$\mathcal{B}(W \to \ell\nu_\ell)/\mathcal{B}(W \to \mu\nu_\mu)$ for both lepton charges and to compute the average. The analysis strategy in both final states in similar: the cross-section is measured in eight bins of pseudo-rapidity per lepton charge from a binned maximum likelihood template fit to the transverse momentum of the lepton. Once the production cross-sections are known, the ratio of branching fractions $\mathcal{B}(W \to e\nu_e)/\mathcal{B}(W \to \mu\nu_\mu)$ is computed. As the upper kinematic bounds in pseudorapidity η differ for $W \to \mu\nu_\mu$ and $W \to e\nu_e$, the test of lepton flavour universality is restricted to $2.00 < \eta < 3.50$ and the ratios are found to be

$$\frac{\mathcal{B}(W^+ \to e^+\nu_e)}{\mathcal{B}(W^+ \to \mu^+\nu_\mu)} = 1.024 \pm 0.003 \pm 0.019, \tag{1.62}$$

$$\frac{\mathcal{B}(W^- \to e^-\overline{\nu}_e)}{\mathcal{B}(W^- \to \mu^-\overline{\nu}_\mu)} = 1.014 \pm 0.004 \pm 0.022, \tag{1.63}$$

$$\frac{\mathcal{B}(W \to e\nu_e)}{\mathcal{B}(W \to \mu\nu_\mu)} = 1.020 \pm 0.002 \pm 0.019, \tag{1.64}$$

where the first uncertainty is statistical and the second is systematic. The ATLAS Collaboration recently published a measurement finding $\mathcal{B}(W \to e\nu_e)/\mathcal{B}(W \to \mu\nu_\mu) = 0.9967 \pm 0.0004 \pm 0.0101$ [29], which exceeds the previous ATLAS measurements in precision. All measurements are in good agreement and no evidence of lepton flavour universality violation is observed.

Chapter 2

LHC and the LHCb detector

LHCb is one of the four major experiments at the Large Hadron Collider (LHC) [30]. The LHC is an accelerator and a circular collider, situated near Geneva, across the French-Swiss border, as shown in Fig. 2.1. After a brief introduction about the LHC in Sec. 2.1, a detailed description of the LHCb detector is given in Sec. 2.2. In particular, the LHCb tracking and the particle identification (PID) systems are described in Sec. 2.3 and Sec 2.4 respectively. Finally, the LHCb trigger system is introduced in Sec. 2.5 and the LHCb experiment computing model and data management is described in Sec. 2.6.

2.1 The Large Hadron Collider

The Large Hadron Collider is a two ring hadron accelerator, installed in a 27-kilometre long tunnel, the one where the LEP collider was situated. The LHC is designed to collide protons up to a centre-of-mass energy of 14 TeV, with an instantaneous luminosity of $10^{34}\,\mathrm{cm}^2\,\mathrm{s}^{-1}$, while heavy-ion collisions, such as Pb-Pb, happen at a centre-of-mass of 2.8 TeV per nucleon with a peak luminosity of $10^{27}\,\mathrm{cm}^2\,\mathrm{s}^{-1}$. Until now, the LHC has collided protons at $\sqrt{s} = 7$ TeV in 2010-2011, $\sqrt{s} = 8$ TeV in 2012 and $\sqrt{s} = 13$ TeV since 2015.

The protons used in collisions are obtained from ionized hydrogen atoms. Then, since it is not possible to accelerate the protons from quasi-rest condition up to the required energy, they are accelerated in consecutive steps. A complex system of machines is used in the acceleration process, as shown in Fig. 2.2. In the first step the protons are injected in the Linac2, a linear accelerator which provides the Proton Synchrotron Booster (PSB) with 50 MeV proton bunches. The PSB can accelerate protons at energies up to 1 GeV. After this, the protons are injected in the Proton Synchrotron (PS), reaching an energy of 26 GeV. Then, they are passed to the Super Proton Synchrotron (SPS) where they are accelerated up to an energy of 450 GeV, before being finally injected to the LHC via two tunnels: TI2 and TI8. The two beams are manteined in their respective orbits thanks to a magnetic field of 8.34 T, generated by superconductive magnetic dipoles kept

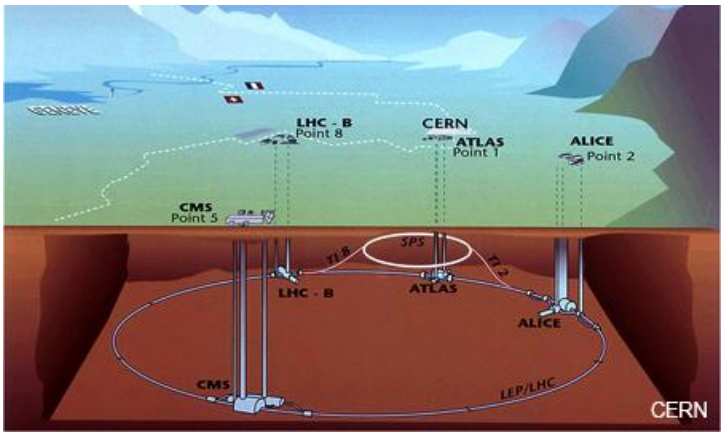

Figure 2.1: View of the LHC and the four major experiments: ALICE, ATLAS, CMS, LHCb.

at a temperature of 1.9 K (−271.3 °C). At the nominal operation regime, the LHC rings store 2808 proton bunches per ring, each one containing about 1.1^{11} protons, colliding at a 40 MHz frequency (*i.e.* a collision every 25 ns).

The LHC has performed very well in these years of data-taking, allowing the LHCb experiment to collect more than 3 fb^{-1} of data both in Run-1 and Run-2 [31]. Furthermore, due to the large $b\bar{b}$ production cross-section, about 500 μb at 14 TeV [32], LHC is the most coupious source of B mesons in the world. This allows the LHCb experiment to perform high precision measurements, improving the previous results coming from the BaBar, Belle and CDF collaborations and hopefully discovering new physics effects in the charm and beauty sectors.

2.2 The LHCb detector

The LHCb experiment [33] is dedicated to heavy flavour physics measurements. Its primary goal is to look for indirect evidence of new physics in *CP*-violating processes and rare decays of beauty and charm hadrons. Due to the average imbalance in momentum of the two partons, the outcoming b quarks are strongly boosted along the beam-line. As a consequence, the B hadrons at the LHC are produced in the same forward or backward emisphere and with a small angle with respect to the beam direction. In order to exploit this feature, the LHCb detector has the structure of a forward spectrometer, in contrast to other LHC experiments. Its geometrical acceptance lies between 10 and 300 mrad in the horizontal plane (x-z) and between 10 and 250 mrad in the vertical plane. The difference between horizontal and vertical acceptances is justified by the fact that the horizontal plane is also the bending plane for charged particles deflected by the dipole

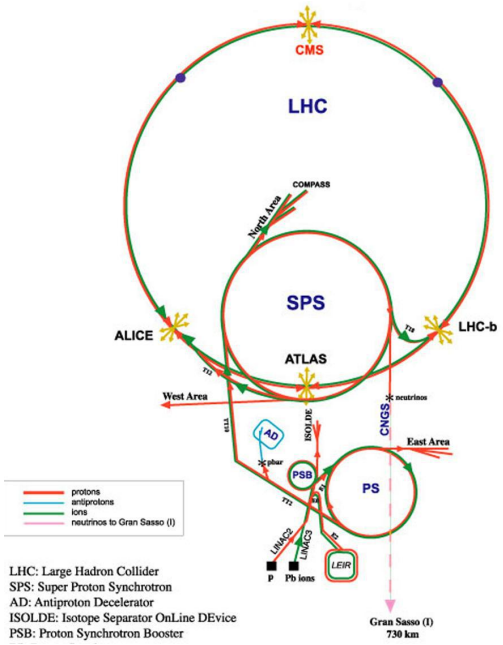

Figure 2.2: Scheme representing the various machines employed to pre-accelerate the protons that will be injected in the LHC. From the bottom, in order: proton injector, LINAC2, PSB, PS, SPS.

magnetic field of the LHCb detector. The pseudorapidity[1] (η) range for tracks inside the LHCb geometrical acceptance is between about 1.8 and 4.9.

To fulfill the LHCb physics program, the detector must have the following characteristics:

- a great precision in the reconstruction of the interaction vertices and of the B and D hadrons decay vertices. For example, an excellent proper-time resolution is fundamental to measure the neutral B mesons oscillations;

- an excellent PID system. In order to identify hadronic B and D decays, an excellent discrimination between charged pions, kaons and protons with momentum between few GeV/c up to 150 GeV/c is required;

- the invariant-mass resolution must be as small as possible in order to discriminate the signals from the combinatorial background and to distinguish between B^0 and B_s^0 signal peaks. For these reasons, the momentum of charged tracks must be measured with a relative precision of about 10^{-3};

- the trigger system must be able to reject a very large part of the background, in order to have manageable data-sample. Since the production cross-sections of c

[1]The pseudorapidity is defined as $\eta = -\ln\tan\left(\frac{\theta}{2}\right) = \frac{1}{2}\ln\frac{|\vec{p}|+p_L}{|\vec{p}|-p_L}$, where θ is the angle between the particle and the beam axis and p_L the longitudinal momentum.

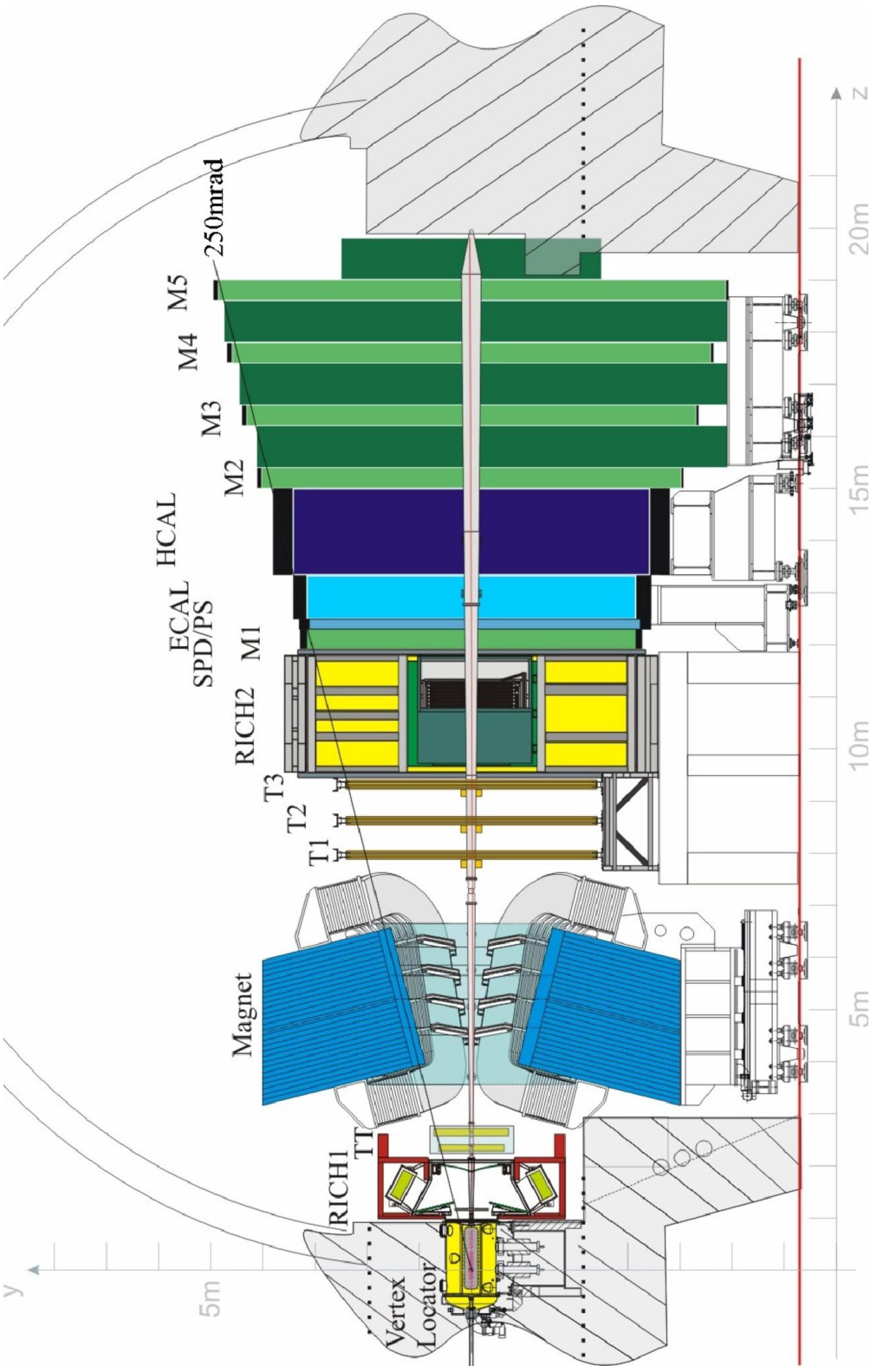

Figure 2.3: Schematic view of the LHCb detector. From left to right the various sub-detectors are visible: VELO, RICH1, TT, Magnet, the three Tracking Stations, RICH2, Electromagnetic Calorimeter (ECAL), Hadronic Calorimeter (HCAL) and Muon Stations [31].

and b quarks together account for nearly 10% of the total pp inelastic cross-section (*i.e.* one collision out of ten produces D or B hadrons), the trigger system needs to be flexible and efficient. To achieve this, the LHCb trigger is organized in multiple levels, each of them more specialized (but slower) than the previous;

- efficient and reliable computing resources, needed for both the processing and the storage of data.

In Fig. 2.3 a schematic view of the LHCb detector is represented. The various sub-detectors are visible. They can be divided in two categories: the tracking and the PID systems.

Tracking systems: VELO (VErtex LOcator), Trigger Tracker (TT) and T1-T3 stations. The VELO is a system which identifies the primary and secondary interaction vertices and it is situated around the beam interaction point. The Trigger Tracker (TT) is placed behind the first RICH. Each of the three stations, placed after the magnet, is divided in two parts, the Inner Tracker (IT), which together with the TT forms the Silicon Tracker (ST), and the Outer Tracker (OT). The ST and OT tasks are the reconstruction of the tracks and the measurement of the particle's momentum.

PID systems: two Ring Imaging Cherenkov detectors (RICH1 and RICH2), two calorimeters (ECAL and HCAL) and five muon stations (M1–M5). RICH1, the first Cherenkov detector, is placed immediately after the VELO, while the second, RICH2, is placed after the Tracking Stations. The main task of the two RICH detectors is the discrimination of pions, kaons, and protons with momenta up to 150 GeV/c. The calorimeters system is divided in four sub-detectors: Scintillator Pad Detector (SPD), Pre-Shower (PS) and Electromagnetic and Hadronic calorimeters (named ECAL and HCAL, respectively). The system measures the energy of the particles that hit the sub-detectors. While the ECAL measures e^+, e^- and γ energies, the HCAL measures the hadrons energies. At the end of the LHCb detector, five MultiWire Proportional Chambers (MWPCs), spaced with iron filters, are used to identify muons.

A detailed description of the tracking and PID systems is given in Secs. 2.3 and 2.4, respectively.

2.3 The LHCb tracking system

The tracking system is dedicated to identify the primary and secondary interaction vertices, to reconstruct the trajectories of charged particles and to measure their momentum exploiting a magnetic bending field generated by a warm magnetic dipole. The first

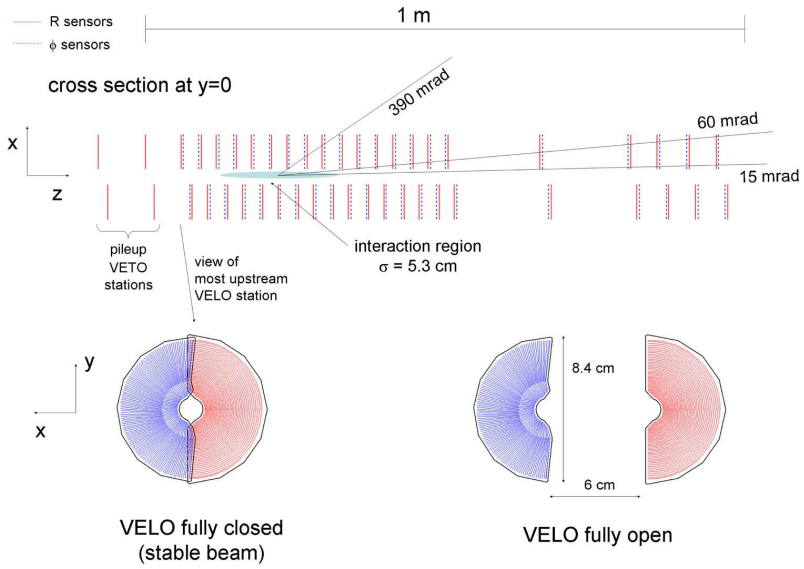

Figure 2.4: Top view of the VELO sub-detector. Frontal view of the modules in the closed (bottom left) and open positions (bottom right).

task is performed by the VELO, which, together with the rest of the tracking system, is also used for the track reconstruction.

2.3.1 The Vertex Locator

A vertex detector with a micrometric precision is fundamental for the reconstruction of the primary and secondary interaction vertices. Indeed, the main signature of B-hadrons decays at LHCb is the large mean distance of flight, tipically about 1 cm. For this reason, measuring with high precision the position of a secondary vertex well displaced from the pp primary vertex is very important, since it allows to select signal events and reject most of the background in a high multiplicity environment.

The VELO [34,35] is composed of 21 circular silicon modules, installed perpendicularly along the beam line, as shown in Fig. 2.4. Each silicon module is divided in two halves in order to allow the positioning of the VELO during different phases of the experiment. As can be seen in the bottom part of Fig. 2.4, during the data-taking phase the VELO is closed, while during the beam-stabilisation one it is open. For this reason, the modules are installed on a movable device placed inside a vacuum vessel. In order to achieve a better geometrical coverage, the two halves of a module partly overlap in the closed VELO configuration, as shown in Fig. 2.4. The modules are composed by two planes of 220 µm thick silicon micro-strip sensors, able to measure the radial distance from the beam (R) and the polar angle (ϕ) of hits generated by the ionizing particles that cross

the VELO. The coordinate z is simply measured knowing what module gives a signal for a particular hit.

The R sensors are divided into four parts per half, each one covering about 45°. The micro-strips composing these are modeled in a semi-circular shape and their width increases as the distance from the center becomes greater, because the majority of the particles is expected to be near the beam axis (*i.e.* in high η regions). The micro-strips width ranges from 40 µm near the center to 92 µm far from the beam.

The ϕ sensors are divided in an inner and in an outer region. The latter starts at a radius of 17.25 mm and its pitch is set to be roughly half (39.3 µm) than that of the inner region, which is 78.3 µm and ends at the same radius. In order to improve pattern recognition, the two regions have different skew to the radial direction: the inner one is tilted by 20° and the other by 10°. Furthermore, to improve the track reconstruction, the longitudinally adjacent ϕ sensors have opposite skew to each other.

The performances of the VELO detector have been analyzed using the the data collected in 2010 and 2011. The resolution on the x and y coordinates ranges from 40 µm to 10 µm depending on the number of tracks used to form a vertex, while the resolution on the z coordinate ranges from 250 µm to 50 µm, for the same reason.

2.3.2 Silicon Tracker (ST)

The Silicon Tracker (ST) is composed by two different detectors that use silicon micro-strip sensors: the Trigger Tracker (TT) and the Inner Tracker (IT) [36].

The Trigger Tracker (TT) is situated after the first Ring Imaging Cherenkov detector and before the magnet. The TT's goal is to provide reference segments used to combine the track reconstructed in the tracking stations with those reconstructed in the VELO, in order to improve the momentum and coordinate resolution. Since an integrated magnetic field of 0.15 Tm is present in the space between the VELO and the TT station, the track transverse momentum can be estimated with a resolution of $\delta p_{\mathrm{T}}/p_{\mathrm{T}} = 25\%$ at $p_{\mathrm{T}} = 1$ GeV/c. The system is composed by four stations, divided in two groups called respectively TTa and TTb, at a distance of about 30 cm one from the other and placed approximately 2.4 m after the beam interaction region. A detailed scheme of this part of the LHCb detector is shown in Fig. 2.5. Each of the four stations covers a rectangular region of about 120 cm in height and about 150 cm in width. In the first and fourth stations the strips are parallel to the vertical plane, while in the second and third stations they are tilted by +5° (u-layer) and −5° (v-layer) respectively, in order to improve the precision of the track reconstruction.

The Inner Tracker is composed by the three inner parts of the stations T1, T2 and T3. Each IT station is arranged around the beam pipe and consists of four individual detector boxes, each one containing four detection layers. Each detection layer is composed by seven detector modules and each module is formed by one or two silicon sensors and a

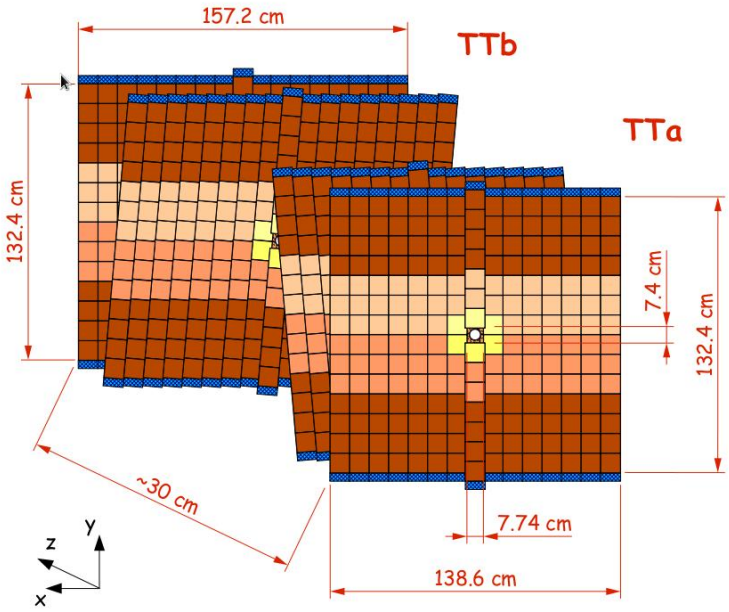

Figure 2.5: View of the Trigger Tracker detector. The first and fourth stations have sensors parallel to the vertical plane, while the second and third stations (called u-plane and v-plane) have sensors tilted respectively by $+5°$ and $-5°$.

readout hybrid. The detection layers are positioned in the same way as the TT. On the other hand, the side boxes have to two ladders of micro-strips, with those of the lower sensor connected in series with those of the upper sensor to a single readout channel, while the top and bottom boxes have only one micro-strips ladder. The total IT size is about 1.2 m in the bending plane and about 40 cm in the vertical plane.

2.3.3 The Outer Tracker (OT)

The Outer Tracker [37] is a gas-filled straw tube detector, covering about 99% of the summed surface of the T1-T3 tracker stations. For each tracking station there are four planes of straw tubes arranged in the same way as the TT and IT silicon micro-strip sensors: the first and the fourth with tubes parallel to the vertical plane, while the second and the third with tubes tilted by $\pm 5°$ (u-layer and v-layer). Each plane is composed of two rows of tubes, arranged in a honeycomb structure. These tubes have a radius of 5 mm and are filled with a mixture of $Ar/CF_4/CO_2$. The anode wire is supported and centred with a precision better than 100 µm by locator pieces at the tube ends. Unlike other tracking detectors here described, the OT measures drift times rather than pulse heights. Due to the limited drift speed of the gas mixture, the readout time window exceeds a single LHC bunch crossing interval. The OT spacial resolution is better than 200 µm.

2.3.4 The LHCb dipole magnet

In every modern high-energy experiment, momenta are measured through the particles curvature in a given magnetic field. In particular, the LHCb detector is provided with a warm[2] magnet dipole [38] placed between the TT and the first tracking station T1, as can be seen in Fig. 2.3. The magnet geometry has been chosen considering the detector acceptance. The magnet is formed by two coils shaped in order to become wider as the z coordinate increases, as can be seen in the top part of Fig. 2.6. The magnetic field is oriented along the y coordinate, perpendicular to the x-z plane, referred to as the bending plane. The maximum intensity of the magnetic field is about 1 T, and the magnetic field integral is 4 Tm. In order to allow the evaluation of any left-right asymmetry in the detector, the polarity of the magnetic field has been flipped several times during the data-taking.

2.3.5 Tracking algorithm and performances

In the development of the kinematic fit the tracking performance is of great importance. The trajectories of the charged particles traversing the tracking system are reconstructed from hits in the VELO, TT, IT and OT detectors. As illustrated in Fig. 2.6, the tracks are divided in five categories:

Long tracks: particles generating hits in all tracking sub-detectors.

VELO tracks: particles generating hits only inside the VELO. Since these tracks have a wide angle with respect to the beam pipe, they exit from the detector geometrical acceptance just after the VELO.

Upstream tracks: tracks generated by particles with a low momentum. These produce hits in the VELO and in the TT, but they are kicked off the geometrical acceptance of the detector by the magnetic field generated by the warm magnetic dipole. It is possible to measure their momentum thanks to the residual magnetic field present in the VELO, even if the measurement is affected by a 20% relative uncertainty.

Downstream tracks: Long lived neutral particles can decay between the VELO and the TT, producing charged particles that generate hits in the TT and in the three tracking stations.

T tracks: tracks which have hits only in the tracking stations are classified as T tracks.

Track finding and reconstruction are organized in different steps. The first one starts with the definition of segments in the various sub-detectors. Inside the VELO, segments are

[2] A warm dipole is made of non superconducting material, so it does not requires very low temperatures to work.

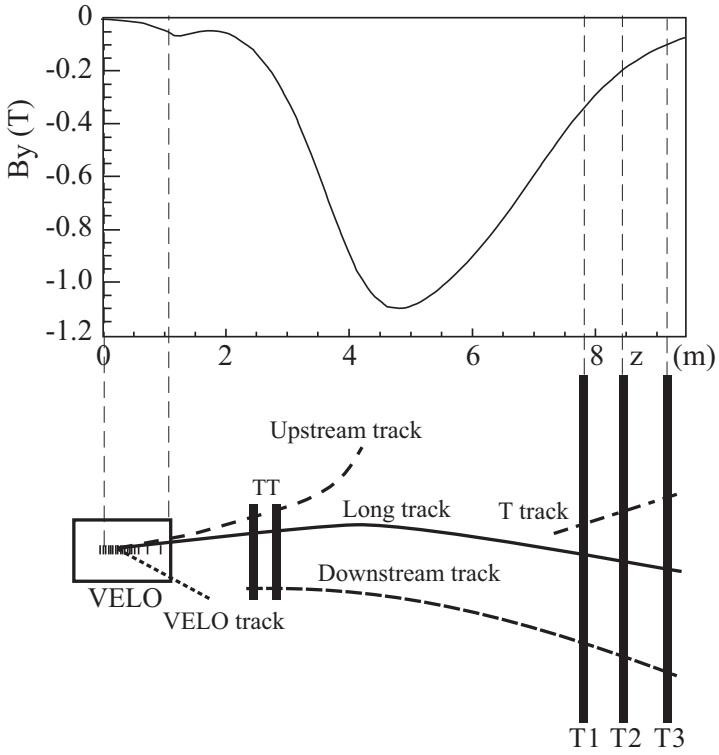

Figure 2.6: A schematic illustration of the various track types [33]: long, upstream, downstream, VELO and T tracks. The main magnetic field component (B_y) is plotted above as a function of the z coordinate, for reference.

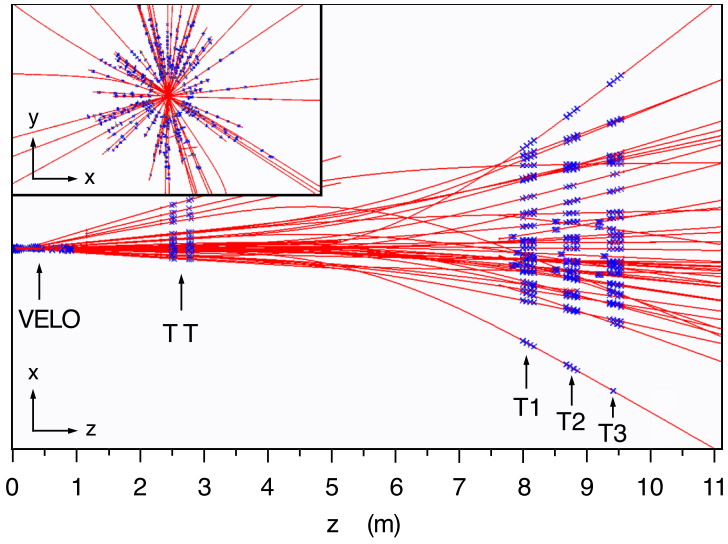

Figure 2.7: Display of the reconstructed tracks (red) and assigned hits (blue) in an event in the $x-z$ plane [33]. The insert shows a zoom into the VELO region in the $x-y$ plane.

created matching all hits lying on a straight line. In the tracking stations, a segment is created matching the hits contained in a section of T1 and T3 (*e.g.* in the left corner on these two stations), using the information given only by one plane of vertically oriented micro-strip sensors. Then, under the hypothesis of a parabolic trajectory, the algorithm calculates the position of the hit in the middle stations and searches for compatible hits. If a signal is found, it is added to the segment and it is used to better determine the parameters of the trajectory. Finally, in order to have a 3-dimensional segment, the compatible hits coming from the u-plane and the v-plane are also added.

On the other hand, the reconstruction process is organized in a hierarchical way. First of all, the algorithm tries to reconstruct long tracks and then it picks up unused segments to reconstruct downstream and upstream tracks, as follows.

- Long tracks are reconstructed with two algorithms. The first one extrapolates VELO segments to the tracking stations, adding to the track the compatible hits in the TT. The second matches VELO and tracking stations segments one to each other, extrapolating VELO segments in the forward direction and tracking stations segments in the backward direction.

- Downstream tracks are reconstructed starting from T stations segments and then adding the compatible hits in the TT to those segments.

- Upstream tracks are obtained extrapolating VELO segments to the Trigger Tracker, adding compatible hits and requiring a non compatibility with any of the tracking station segments.

In a final step, the tracks are fitted using a Kalman filter. The fit takes into account multiple scattering and corrects for energy loss due to ionisation. The χ^2 per degree of freedom of the fit is used to determine the quality of the reconstructed track. After the fit, the reconstructed track is represented by state vectors, specified at given z-positions in the experiment,

$$\vec{\alpha} = \left(x, y, \frac{dx}{dz}, \frac{dy}{dz}, \frac{q}{|\vec{p}|}\right)_z \tag{2.1}$$

where q is the particle charge and x, y, z are the spacial coordinates. Moreover, if two or more tracks have many hits in common, only the one with most hits is kept. In Fig. 2.7 the tracks reconstructed in a typical event (red) and the hits in the detector (blue) are shown in the bending plane ($x - z$) and in the $x - y$ plane.

Mis-reconstructed (fake or ghost) tracks are those that do not correspond to the trajectory of a real charged particle. Because of the large extrapolation distance in traversing the magnet, most of these fake tracks originate from wrong associations between VELO tracks and tracks in the T stations. The fraction of fake tracks in minimum bias events is typically around 6.5%, increasing to about 20% for large multiplicity events [40].

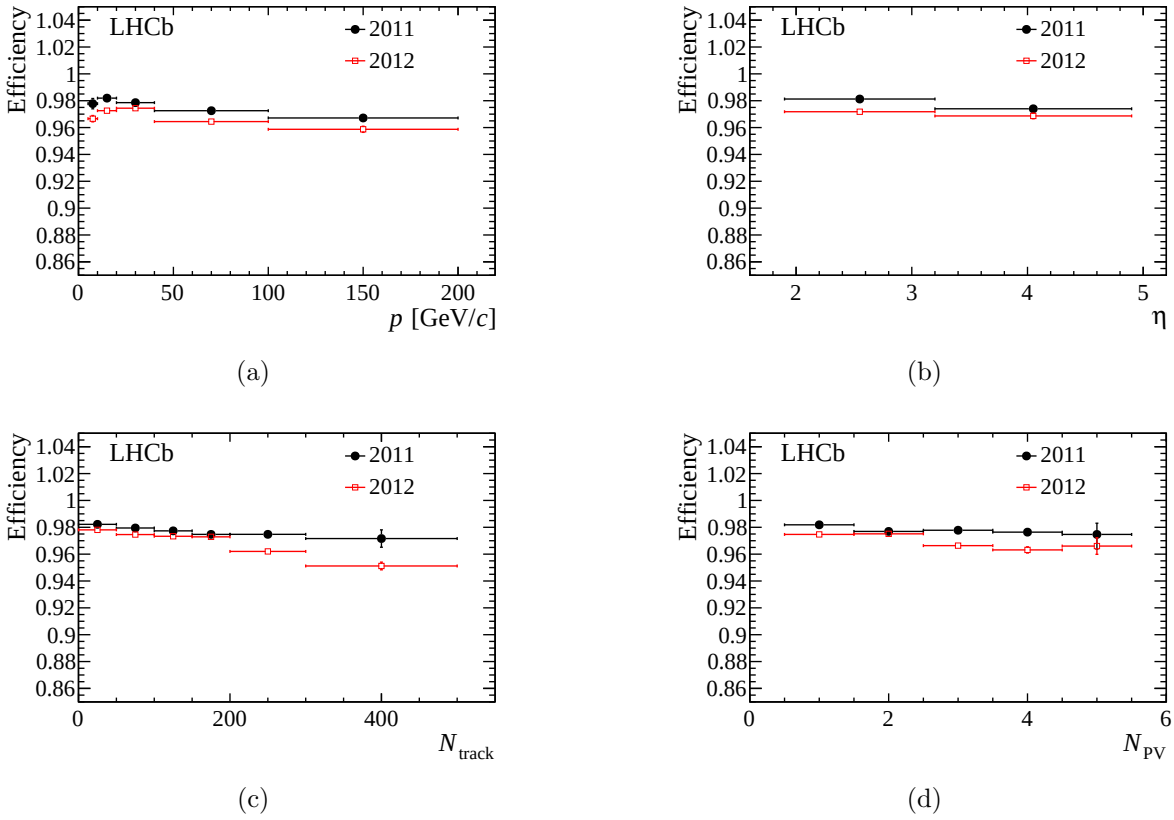

Figure 2.8: Tracking efficiency as function of the (top left) momentum, (top right) the pseudorapidity, (bottom left) the total number of tracks in the event (N_{track}) and (bottom right) the number of reconstructed primary vertices (N_{PV}) [39]. The error bars indicate the statistical uncertainty.

To reduce this fake rate, a neural network classifier is used, at the cost of a small drop in efficiency. This uses as input the result of the track fit, the track kinematics and the number of measured hits in the tracking stations versus the number of expected hits.

The tracking efficiency is defined as the probability that the trajectory of a charged particle that has passed through the full tracking system is reconstructed. In particular, this efficiency does not account for interactions with the material, decays in flight and particles that fly outside of the detector acceptance. The efficiency is measured using a tag-and-probe technique with $J/\psi \rightarrow \mu^+\mu^-$ decays. In this method one of the daughter particles, the "tag" leg, is fully reconstructed, while the other one, the "probe" leg, is only partially reconstructed.

The overall efficiency depends on the momentum spectrum of the tracks and the track multiplicity of the event. The tracking efficiency, measured in 2011 and 2012 is shown in Fig. 2.8 (in black and red, respectively) as a function of various quantities. The performance in 2012 is slightly worse, which is partially due to the higher hit multiplicity at the higher centre-of-mass energy. As can be seen, the average efficiency is above 96% in the momentum range 5 GeV/c $< p <$ 200 GeV/c and in the pseudorapidity range $2 < \eta < 5$, which covers the phase space of LHCb. Only in high multiplicity events ($N_{\text{track}} > 200$) the efficiency is slightly less than 96%. The track reconstruction efficiency has been shown to be well reproduced in simulated events [39].

2.4 The LHCb particle identification system

In this section all the sub-detectors installed in the LHCb detector used for the particle identification are described. The LHCb PID system includes two Ring Imaging Cherenkov detectors (RICH1 and RICH2), the electromagnetic calorimeter (ECAL), the hadronic calorimeter (HCAL) and finally the muon detector.

2.4.1 The RICH detectors

For the discrimination of charged pions, kaons and protons in a momentum range between few GeV/c up to about 150 GeV/c, two Ring Imaging Cherenkov detectors are used: RICH1, installed immediately after the VELO, and RICH2, positioned after the tracking stations [41].

Cherenkov light detectors exploit the light emitted by particles that travel in a medium faster than the light in the same medium. The relation between the Cherenkov photon emission angle θ_C and the refraction index n of the radiator is:

$$\cos(\theta_C) = \frac{1}{\beta n} \tag{2.2}$$

where $\beta = v/c$ is the particle velocity with respect to the speed of light in vacuum. From this relation, it is possible to notice that Cherenkov light is emitted only by those particles with $c/n < v < c$. For instance, if $v = c/n$ then $\cos(\theta_C) = 1$ and so $\theta_C = 0$, while if $v = c$ then $\cos(\theta_C) = 1/n$ and so $\theta_C = \arccos(1/n)$. Thus, it is evident that for particles approaching the speed of light the Cherenkov angle will saturate at the value $\theta_C = \arccos(1/n)$. For these reasons, it is necessary to have different radiators in order to discriminate particles in a wide range of momenta.

RICH1 is optimized to identify tracks with a medium-low momentum, between 1 GeV/c and about 50 GeV/c. The structure of the apparatus is reported in the left part of Fig. 2.9. The RICH1 is placed immediately after the VELO and its geometrical acceptance (between 25 mrad to 330 mrad) is enough to cover practically the whole LHCb detector acceptance. There are two different types of radiators inside RICH1: the first is a 5 cm thick Aerogel layer, with $n = 1.03$, suitable for low momentum particles, the second radiator is gaseous C_4F_{10} ($n = 1.0015$) filling the remaining part of the detector and is employed to detect particles with higher momenta (up to 50 GeV/c).

RICH2, instead, is placed behind the last tracking station. Its geometrical acceptance, 120 mrad in the vertical plane and 100 mrad in the horizontal plane, covers the region of the detector where most of high momentum particles are found. The radiator chosen is gaseous CF_4, with a refraction index $n = 1.00046$, optimal for the higher momentum region, up to about 150 GeV/c. A schematic view of the two sub-detectors is visible in Fig. 2.9.

Thanks to a system composed of spherical and plane mirrors, the Cherenkov photons emitted in both detectors are conveyed onto a lattice of photo detectors, the Hybrid Photon Detectors (HPDs). The HPDs are placed in both the sub-detectors outside the LHCb detector acceptance and they are shielded against the residual magnetic field. This feature is particularly important for RICH1, since in this region of the LHCb detector the residual magnetic field is not negligible. The shielding is necessary in order to allow the HPDs to operate properly, since the photo-electrons created in the photomultipliers could be bent by the residual magnetic field and this would reduce the HPDs performances. This configuration allows to have optimal results with signal's rise and fall times of about 1 ns.

2.4.2 Particle identification method

RICH detectors are able to discriminate between the various mass hypotheses for a given particle, since the photon emission angle is related to the particle mass and to its momentum. As the emission covers the full solid angle, rings on the HPD plane, with radius proportional to θ_C, are expected. The hits on the HPD plane will be distributed around a particular radius value, corresponding to the Cherenkov emission angle. Due to resolution effects, the distribution will be smeared around the central value. By measuring

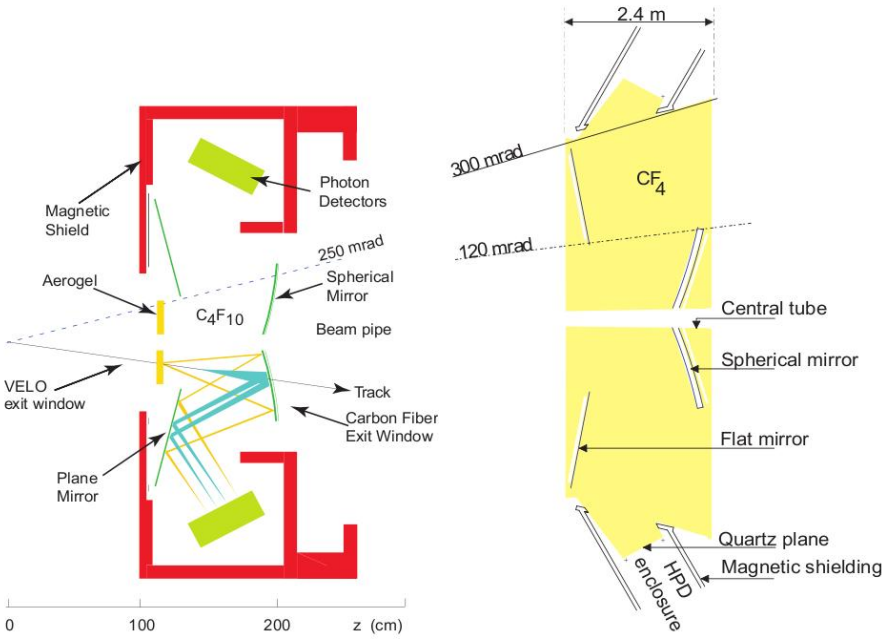

Figure 2.9: Overview of the two RICH sub-detectors. On the left the RICH1 is represented. It is relevant to note the different Cherenkov photon emission angles of the Aerogel (yellow) and C_4F_{10} (light blue) radiators. On the right the RICH2, filled with CF_4 gas, is represented.

the photons hit positions, it is possibile to obtain a value of θ_C for each particle, allowing the discrimination between the various mass hypotheses.

Because of an irreducible background given by photons coming from other particles and the complexity of the problem, the following approach has been chosen to achieve the best particle discrimination performances. For a given set of mass hypotheses, the probability for a single photon to be detected on a single HPD pixel is computed. After that, the expected contribution from all sources is compared with the observed number of photons and a likelihood is calculated, whose change in value depends only on the mass hypotheses assigned to the tracks. Only five mass hypotheses are considered for the tracks detected: electron, muon, pion, kaon and proton.

The pion mass-hypothesis is used for all the tracks detected and a first global likelihood is computed. Then, the hypothesis is changed to e, μ, K and p for one particle at a time and the change in the global likelihood is computed. The chosen mass hypotheses is the one that returns the maximum improvement in the global likelihood. This process is repeated for all tracks, until no improvement is observed in the likelihood value.

The discriminating variable is the difference between the logarithm of the likelihood for the particle P under two particle hypotheses, $\Delta \log \mathcal{L}(P)$. For example, $\Delta \log \mathcal{L}_{K-\pi}(P)$ is the difference between the logarithm of the likelihood under the K and π hypothesis

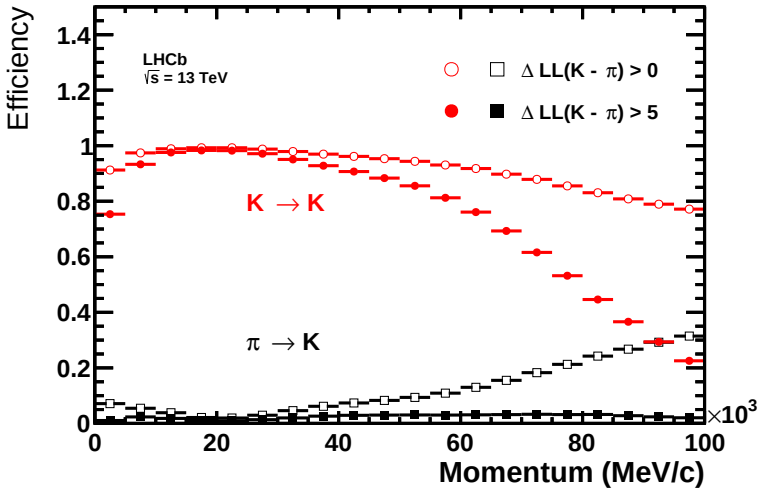

Figure 2.10: Kaon ID performance for 2015 dataset. The efficiency for the identification of kaon $K \to K$ (red) and the mis-ID of pions as kaons $\pi \to K$ (black) as a function of the momentum are represented, for different requirements in the likelihood difference [42].

for the particle P

$$\Delta \log \mathcal{L}_{K-\pi}(P) = \log \mathcal{L}_K(P) - \log \mathcal{L}_\pi(P). \tag{2.3}$$

A large positive value of $\Delta \log \mathcal{L}_{K-\pi}(P)$ corresponds to a high probability that the particle P is a kaon, while a large negative value of $\Delta \log \mathcal{L}_{K-\pi}(P)$ corresponds to a high probability that the particle P is a pion.

Another useful discriminating variable is the so-called `ProbNNpi(K,...)`. This quantity represents the probability, computed through a MC-trained neural network, for a detected particle to be a pion (kaon,...). This variable will be used in the process of the background evaluation in Chapter 4.

The efficiency of these discrimination methods has been widely studied using calibration data samples with high purity final states selectable only using kinematical requirements, without using the RICH sub-detectors information. Due to their particular kinematic characteristics $K^0_S \to \pi^+\pi^-$, $D^{*+} \to D^0(K^-\pi^+)\pi^+$ and $\Lambda \to p\pi^-$ are used as calibration samples. In Fig. 2.10, the kaon ID and the pion mis-ID efficiencies are reported. Since θ_C depends on the particle momentum, the efficiency and the mis-identification are plotted as a function of the momentum. In particular, the efficiency for correctly identified particles, such as kaons, is represented in red, while the pion mis-identification rate is shown in black.

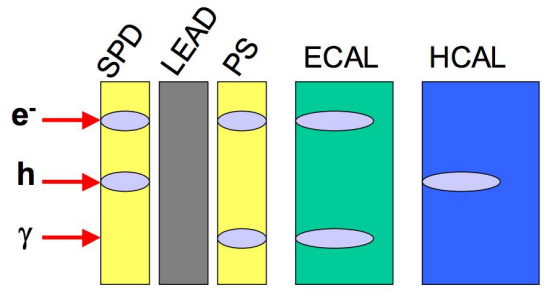

Figure 2.11: Schematic representation of the signal deposited on the different parts of the calorimeter by an electron, an hadron and a photon.

2.4.3 The calorimeters system

The calorimeters system is used to measure hadrons, electron and photon energies. As a consequence, it gives information for their identification and it provides important information for the Level-0 (L0) trigger, evaluating hadron, electron and photon transverse energy E_{T}. The calorimeter system is divided into four subdetectors [43]

- Scintillator Pad Detector (SPD);
- Pre-Shower (PS);
- Electromagnetic Calorimeter (ECAL);
- Hadronic Calorimeter (HCAL).

The calorimeters system and its interactions with particles is schematically represented in Fig. 2.11. Each sub-detector is divided into regions with different dimensions and sensors sizes. In order to reach a compromise between occupancy and the number of read-out channels, the sensor size increases with the distance from the beam pipe. In particular, SPD, PS and ECAL are divided in inner, middle and outer regions, while HCAL is divided in two parts (inner and outer). The SPD and the PS are auxiliary sub-detectors of the electromagnetic calorimeter and they are placed in front of it.

In particular, the SPD is used to discriminate between charged and neutral particles, since the former emit light when crossing a scintillator material while the latter do not. On the other hand, the PS is used to obtain a better discrimination between electrons and pions. Both the SPD and the PS consist of about 6000 scintillating pads with a thickness of 15 mm, interspaced with a 2.5 radiation lengths[3] lead converter. The light produced by the scintillator material is collected using wavelength-shifting fibers (WLS). These

[3] The radiation length is defined as

$$X_0 = \frac{A \cdot 716.4 g/cm^2}{Z(Z+1)\ln(287\sqrt{Z})} \tag{2.4}$$

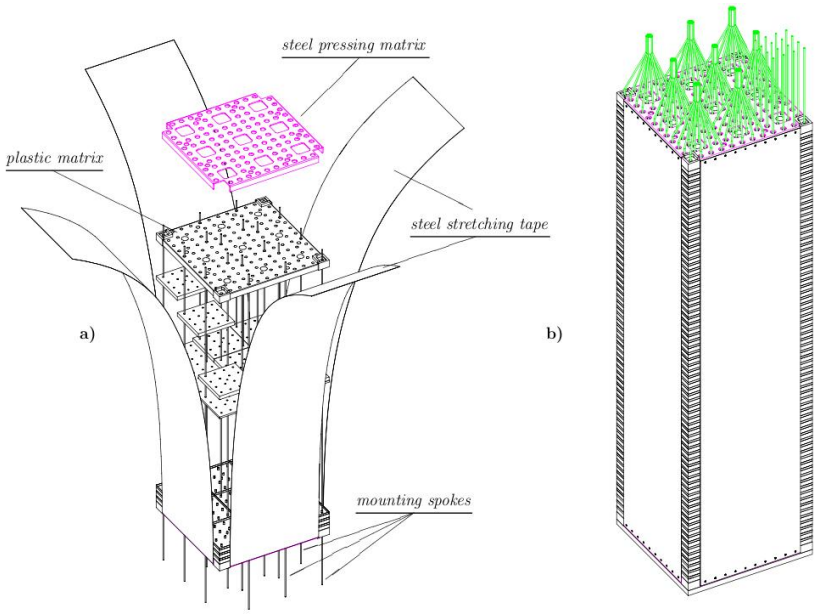

Figure 2.12: Scheme of the ECAL. On the left, an ECAL module during the assembly phase is represented: the lead/scintillator layers are clearly visible. On the right there is a representation of an assembled ECAL module is shown. The green lines connected to an end of the module are the WLS fibers connecting the calorimeter to the photomultipliers.

WLS fibers are used to transmit the light to multi-anode photomultipliers (MAPMTs) located outside the detector.

The ECAL is a sampling calorimeter realized using Shashlik technology and separated in independent modules. The Shashlik calorimeters are sampling calorimeters in which the scintillation light is carried out via WLS fibers running perpendicularly to the converter/absorber plates [45,46]: this technique offers the advantages of an easy assembly, good hermiticity and fast time response. An overview of ECAL is given in Fig. 2.12. Each ECAL module is composed of 66 lead converter layers (2 mm thick), each one installed between two plastic scintillator layers 4 mm thick. In total, all the layers installed in the ECAL correspond to about 25 radiation lengths and 1.1 nuclear interaction lengths. The WLS fibers bring the light produced by the scintillator material to the read-out photo-multipliers in the back part of the module. As said above, the module size and the number of read-out channels differ depending on the region where the module is installed. In the inner region each module has a section of 4×4 cm^2, with 9 read-out channels per module; the middle region contains modules with a section of 6×6 cm^2 and 4 read-out channels. Finally, the outer region is composed of 12×12 cm^2 modules with one channel each.

where A is the mass number and Z is the atomic number of the material considered. The radiation length corresponds to the distance over which the energy of an electron is reduced by a factor 1/e only due radiation loss. For a discussion see Ref. [44].

The HCAL main task it to measure the energies of hadronic showers, thus providing fundamental information for the Level-0 trigger. The HCAL structure is very similar to that of the ECAL, with the only difference that each module is composed of scintillator layers 4 mm thick, interleaved with steel layers 16 mm thick. This corresponds to roughly 5.6 nuclear interaction lengths in total. In the inner region, the modules have a section of 13×13 cm^2, while in the outer region they have a section of 26×26 cm^2.

2.4.4 Calorimeters system resolution

The calorimeter system performances have been evaluated from many test beams made before the start of the data-taking [47, 48]. Energy resolutions are given by $\sigma(E)/E = (8.5 - 9.5)\%/\sqrt{E} \pm 0.8$ for ECAL and $\sigma(E)/E = (69 \pm 5)\%/E \pm (9 \pm 2)\%$ for HCAL. The ECAL calibration is achieved by reconstructing resonances decaying to two photons like $\pi^0 \to \gamma\gamma$ and $\eta \to \gamma\gamma$. Calibration of the HCAL can be realized by measuring the ratio E/p between the energy E as measured in the calorimeter for a hadron with momentum p, as measured by the tracking system.

2.4.5 Muon detectors

The final part of the LHCb detector consists of five muon stations, which, altogether, form the muon sub-detector [49]. Muons with high p_{T} are fundamental particles since they are used by the tagging algorithm to identify the flavor of the spectator B-hadron produced associated to the signal B-hadron. Moreover, they are present in several final products of B-hadron decays as the "golden channels" $B_s^0 \to J/\psi(\mu^+\mu^-)\phi$, $B_0 \to K_0^*\mu^+\mu^-$, or the rare decay $B_s^0 \to \mu^+\mu^-$. To discriminate muons against the abundant hadronic background, muon candidates are formed from aligned hits in each of the five stations of the sub-detector, shown in Fig. 2.13. These stations (M1-M5) cover an angular acceptance of 300 mrad in the horizontal plane and 200 mrad in the vertical plane. The geometrical efficiency for the detection of muons coming from B-hadron decays is nearly 46%. In order to avoid possible muon multiple scattering effects, which could modify the particle trajectory, the first muon station M1 is placed before the calorimeters. The remaining four muon station (M2-M5) are placed after the calorimeter system, at the end of the LHCb detector.

Each muon station is divided into four regions R1-R4, where R1 is the closest to the beam pipe, as it is represented in the bottom part of Fig. 2.13. The dimension of the chambers and the segmentation of each region increase as the distance from the beam pipe becomes greater. In particular, the segmentation increases in a ratio $1 : 2 : 4 : 8$, as shown in Fig. 2.14. As a consequence, the charged particle occupancy is expected to be about the same in each region.

All the chambers are Multi-Wire Proportional Chambers (MWPC), except for the

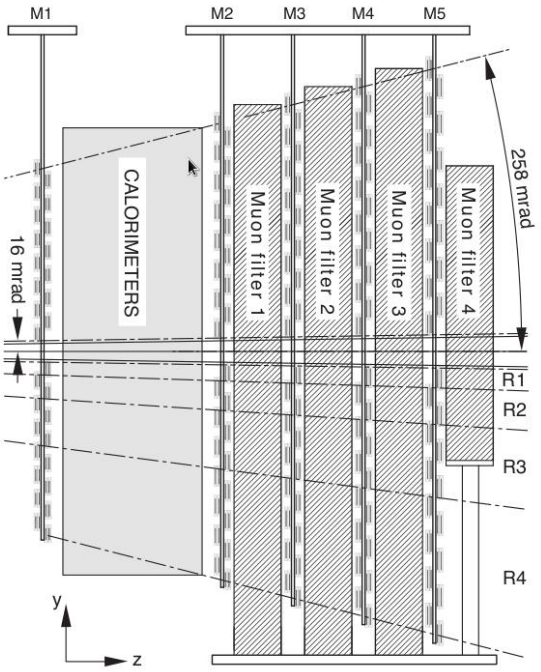

Figure 2.13: Overview of the muon sub-detector in the y-z plane. The five stations sketched are visible. The division in R1-R4 regions is also sketched.

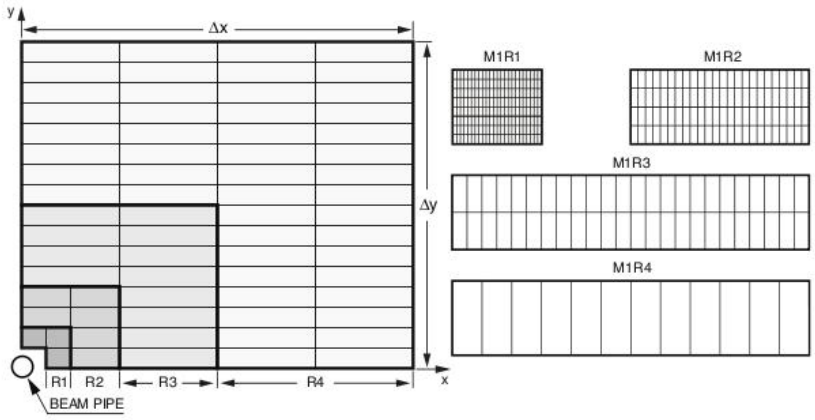

Figure 2.14: On the left, frontal view of a muon station section: each rectangle represents a chamber. Note that they become larger as the distance from the beam pipe increases. Right: different segmentation types of the four chambers. The inner chambers are more segmented than the outer ones.

inner region of the M1 station, where triple-Gas Electron Multiplier (GEM) detectors are employed. MWPCs have four overlapped gaps, each one 5 mm thick and with a distance between wires of about 2 mm. In total, the muon detector contains 1380 MWPCs. The triple-GEM detector consists of three GEM foils sandwiched between anode and cathode planes.

2.4.6 Muon-ID algorithm performances

The muon-ID algorithm in the hardware trigger takes hits in the M3 station as input. For each hit, a straight line is extrapolated to the interaction region defining a "field of interest", taking into account the magnetic field kick around such a trajectory. Hits coming from long and downstream tracks that are found around the extrapolated trajectory are fitted together to form a muon track. The muon identification requires different combinations of hits as a function of the momentum.

- If $3 < p < 3.5$ GeV/c, then hits in M1-M3 are required.
- If $3.5 < p < 4.5$ GeV/c, then hits in M1-M4 are required.
- If $p > 4.5$ GeV/c, then hits in all the five stations are required.

After this, complex algorithms compute the muon likelihood for each muon track, used as a particle-identification discriminator.

2.5 The LHCb trigger system

The production cross-sections of $b\bar{b}$ and $c\bar{c}$ pairs are quite large and this means that a very good trigger system is required, in order to accept only the interesting events while rejecting most of the background events at the same time. The LHCb trigger has been developed to work at the bunch crossing frequency of the LHC, in order to process the largest number of events possible [50].

The only way to reach the desired performances is to divide the trigger into different levels, each processing the output of the previous. In particular, the LHCb trigger system is divided into three levels:

Level-0 (L0): this is the first trigger level and it is based on custom electronics. It is designed to perform a first filtering of the events, reducing the input rate of about 40 MHz to an output rate of only 1 MHz.

High Level Trigger 1 (HLT1): this is the second trigger level and it is software based. HLT1's tasks are to filter events in an inclusive way and to reduce the rate of accepted events to 50 kHz, starting from an input rate of about 1 MHz, given by the L0.

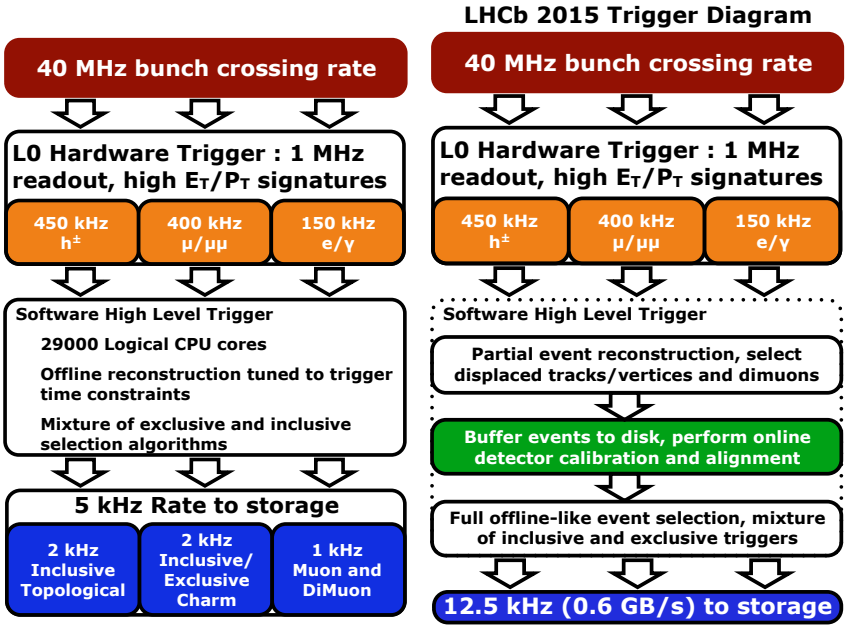

Figure 2.15: The LHCb trigger scheme for Run-1 (left) and Run-2 (right).

High Level Trigger 2 (HLT2): this is the last trigger level and, as the previous one, it is completely software based. The HLT2 takes the input from the HLT1 and reduces it to an output rate of about 12 kHz in Run-2, applying an exclusive selection of beauty and charm decays. The output of HLT2 is finally sent to mass storage.

A summary of the trigger strategies used is reported in Fig. 2.15, where Run-1 strategy is on the left and the Run-2 on the right. Now a detailed description of the various trigger levels is given.

2.5.1 Level-0 Trigger

The L0 trigger uses information coming mainly from the tracking system and from the calorimeters system. In fact, at this level, the trigger decides to keep or discard events based on measurements of p_{T} and E_{T} of the particles composing the event. The system uses three independent systems running in parallel:

- The electron/photon trigger which uses the information given by the SPD/PS and ECAL detectors. Custom boards are programmed to measure the energy of electromagnetic showers. The event is accepted if there is at least one cluster with E_{T} exceeding a given threshold.

- The hadronic trigger, as the name suggests, utilises the information given by the HCAL detector. It works in the same way as the electron/photon trigger: the event is accepted if there is at least one cluster with enough transverse energy.

- The muon trigger uses the information given by the five muon stations. Tracks are reconstructed defining fields of interest around particles hits and then connecting hits in the same field of interest. Events are accepted if at least one muon candidate has a transverse momentum greater than a threshold. Moreover, the trigger contains a line to select muon pairs, asking that the sum of their transverse momenta exceed a given threshold.

Furthermore, since in 2010 and 2011 the detector worked at an input rate four times larger than what planned, a system to reject high-occupancy events was developed and implemented in the L0 trigger. Thanks to its fast response, the SPD can be used to roughly estimate the number of charged particles per event. It has been decided to accept events only if the number of hits in the SPD was less than 600.

2.5.2 The High Level Trigger 1

The HLT1 is devoted to the reduction of the input rate from the L0 trigger to a more manageable level. This is done rejecting events with an OT occupancy larger than 20%, because they would take more than the 25 ms allowed to the HLT1 to take a decision. After this first rough selection, the remaining events are reconstructed, considering that:

- High-mass B hadrons and their production mechanism imply that the particles produced in their decays have larger momentum and transverse momentum compared to other hadrons composed by light quarks.
- The average decay length of B hadrons produced at the LHC is about 1 cm. As a consequence, their decay products will have a large impact parameter (IP) with respect to their primary vertex (PV).
- Each B hadron decay has at least one final state particle with large p, p_{T} and IP.
- VELO reconstruction time is fast enough to allow the full information on the primary vertex to be used by the HLT1.
- The full reconstruction can be performed only for a limited number of tracks, because of the limited time available.

The last two points are the reason why the reconstruction is divided in two steps. In the first step VELO tracks and PV are reconstructed. The tracks are selected requiring large impact parameters with respect to the closest PV and a minimum number of hits in the VELO. If the difference between the expected number of hits and the observed number of hits in the VELO is greater than a certain threshold, the track is rejected. For example, a typical choice of the requirements values used is: IP $> 125\,\mu$m, $N^{\mathrm{hits}}_{\mathrm{obs}} > 9$ and $N^{\mathrm{hits}}_{\mathrm{exp}} - N^{\mathrm{hits}}_{\mathrm{obs}} < 3$. After this, forward reconstructed tracks are further selected, requiring

minimal p and p_{T} thresholds. Finally, remaining tracks are fitted using a bi-directional Kalman filter with outlier removal. This fit is done in order to obtain an offline-quality value for the track χ^2 and an offline-quality covariance matrix at the first state of the track, allowing a cut on the IP significance squared (χ^2(IP)). The requirement on χ^2(IP) is very efficient in rejecting background, while the track χ^2 is suitable in rejecting ghost tracks.

2.5.3 The High Level Trigger 2

HLT2 filtering is mainly based on three inclusive selections, the so-called topological lines. In addition, a few dedicated lines for the LHCb core analyses are used. The main strategy of topological lines is to build multibody candidates in the following way:

- two particles are combined to form a two-body object;
- another input particle is added to the two-body object to form a three-body object and so on;
- the pion mass hypothesis is adopted for all tracks.

In this way, n-body objects are built combining the $(n-1)$-body candidate with another particle (saving CPU time with respect to combining n particles directly). Particles are added to an object only if they respect a cut on the distance of closest approach (DOCA). For example, the two particles forming a two-body object need to have DOCA $< 0.15\,\mathrm{mm}$. When a 3-body object is built combining a 2-body object with another particle, another DOCA $< 0.15\,\mathrm{mm}$ cut is imposed and so on for the construction of further objects. In addition, the HLT2 contains lines which exploit tracks identified as muons. Di-muon candidates are formed and, depending on their mass, selection requirements are applied on the flight distance and p_{T} of the candidate. Single muon candidates are accepted requiring a large p_{T} or a combination of χ^2(IP) and p_{T} requirements.

2.6 Data management and computing

The LHCb computing model is based on a series of distributed multi-tier regional centers of different dimensions. In order to store and process the data coming from the detector and to perform the first selections, the LHCb experiment (as well as the other three major experiments at the LHC) requires large amounts of disk space and CPU power. It is important to note that it would be unfeasible to concentrate the resources needed to perform these tasks in one single place, so the computing system is divided in different tiers dedicated to specific duties. The Tier0, located at CERN, provides to LHCb about 20% of the total resources required by the experiment and it is connected

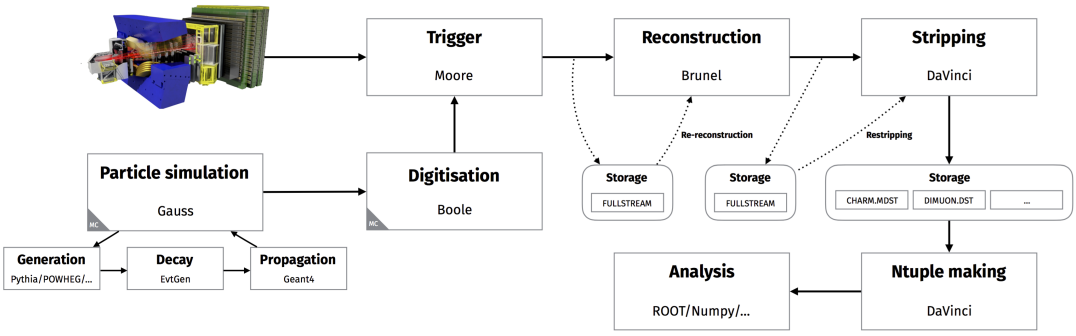

Figure 2.16: The LHCb data flow and the softwares used at each different step.

to the Tier1 centers via 10 Gbit/s optical-fibre links. Moreover, Tier0 stores all the RAW data, also providing a copy distributed among the Tier1 centers. There are 6 LHCb Tier1 centers worldwide that are responsible for storing a proportional share of raw and reconstructed data, as well as performing large-scale reprocessing and storing the corresponding output. Furthermore, the Tier1 centers have to distribute the data to the Tier2 centers and to store a part of the simulated data coming from them. Each Tier1 is connected to a number of Tier2 centres, usually in the same geographical location. Finally, Tier3 resources consist of local clusters in university departments and are dedicated to specific jobs needed by the research team who owns them. This system is collectively referred to as the World LHC Computing Grid (WLCG).

2.6.1 Data processing

The data processing follow a specific flow, designed to maximise the data-taking efficiency and data quality. This consists of several steps, each one being controlled by an 'application' which processes the data event-by-event, using the data from the previous step and creating the results ready for the next. In Fig. 2.16 a schematic overview of these different steps is represented.

The RAW data come from the detector and they are reconstructed via the online Event Filter farm. Then the RAW data are processed using optimized and highly specialized algorithms implemented in the HLTs. The MOORE software applies the necessary calibration corrections during the reconstruction of the properties of the particles and imposes cuts based on physics criteria. After the triggering, raw data are reconstructed by the BRUNEL application in order to transform the detector hits into objects such as tracks and clusters. These objects are stored into an output file in a data summary tape (DST) format, which contains the full event information (reconstructed objects and raw data).

Data are filtered further through a set of selections implemented in the so called *stripping lines*, and applied by the DAVINCI software, which writes out data either in

the DST or micro-DST (μDST) format. In order to save disk space and speed up the access, the output files are grouped into streams which contain similar selections.

For what concerns the simulated data, the events are generated by a MonteCarlo (MC) model considering the pp collisions, the various decays and the LHCb detector response. In particular, the simulated samples are generated using the PYTHIA software [51] to simulate the collision and the hadronization process. Then, the output of the generation phase is processed by the EVTGEN software [52] emulates particle decays. Finally, the propagation of these events in the detector and their interaction with it are simulated by the GEANT4 [53, 54] software.

After the generation and simulation of the detector response, these events are treated in the same way of RAW data, and at the end of the process a DST or a μDST file are written. In addition to the the simulated hits and other interesting quantities, this type of data contain extra "truth" information. The truth information is needed to keep track of physics history of the event and it is carried through all the subsequent processing steps in order to be used during the analysis.

Chapter 3

The Global Fit algorithm

The main goal of this analysis is to realise a preliminary study in order to measure

$$R_{\mu/e} = \frac{\mathcal{B}(D^0 \to K^- \mu^+ \nu_\mu)}{\mathcal{B}(D^0 \to K^- e^+ \nu_e)} \tag{3.1}$$

using the $D^{*+} \to D^0\ (\to K^- \ell^+ \nu_\ell)\pi^+$ decay, where ℓ is either a muon or an electron. Due to the kinematic of the decay and the design of the LHCb detector, the implementation of a global fit (GF) with kinematical constraints has been choosen as a method to reconstruct the neutrino momentum, fundamental for the next steps of the whole analysis. The data samples used in this analysis are the 2015 Run-2 data, corresponding to an integrated luminosity of $0.33\,\text{fb}^{-1}$. The MonteCarlo (MC) samples, produced with the 2015 data taking conditions.

In this Chapter, after the description of the kinematic of the decay (Sec. 3.1) and the analitical reconstruction of the neutrino's momentum (Sec. 3.2), the GF algorithm is described: in Sec. 3.3 the motivations which brought us to this choice, instead of analitically reconstructing $\vec{p}_\nu$, are explained; in Sec. 3.3.1 the statistical method used is described. After this general introduction, the algorithm is described in detail in Sec. 3.4. Finally, some interesting distributions obtained using the outputs of the GF are shown in Sec. 3.6.

3.1 Kinematic of the decay $D^* \to D^0(\to K\ell\nu_\ell)\pi$

In the LHCb detector the $D^{*+} \to D^0\ (\to K^- \ell^+ \nu_\ell)\pi^+$ decay has the topology shown in Fig. 3.1. The D^{*+} meson is produced in the primary pp vertex and it instantaneously decays, through strong interaction, in a D^0 meson and a charged pion. The π flies through the detector, producing a track with a typical momentum of about 5 GeV/c. The D^0 weakly decays after a flight of some centimeters, since it has a mean lifetime $\tau_{D^0} \sim 0.41\,\text{ps}$ and a tipical momentum of about $50\,\text{GeV}/c$.

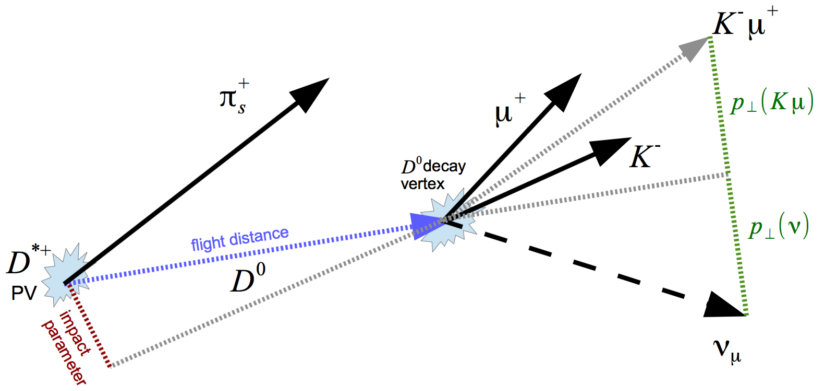

Figure 3.1: Topology of the $D^{*+} \to D^0\ (\to K^-\ell^+\nu_\ell)\pi^+$ decay chain, when $\ell = \mu$. The scale is arbitrary and not realistic.

This secondary vertex, displaced from the pp one, is a typical feature of heavy mesons decays in LHCb and it is necessary to resolve its position with high precision. Another variable useful to discriminate weak decays is the impact parameter (IP), which is the minimum distance between a track and a primary vertex. For example, the pion from the D^{*+} decay, as it comes from the primary vertex, has small IP, while the charged kaon and ℓ are more likely to have large IP values, since they come from a displaced vertex..

Because of its weak interaction with the materials and its neutral electromagnetic charge, the neutrino is not detected in the LHCb. Usually, in detectors with an acceptance region corresponding to the full solid angle and with very precise calorimeters, it is possible to measure the kinematical information of the neutrinos from the total measured energy.

Eve if in the LHCb the information regarding the kinematic of the D^0 decay is only partially known, it is still possible to extract some information about the kinematic of the neutrino. In order to study the decay, in addition to the invariant masses of the D^{*+} and the D^0, it is useful to define other quantities. These are the visible D^0 mass, the corrected D^0 mass and the mass of the $D^0\pi^+$ pair:

- the visible D^0 mass is the invariant mass of the $K\ell$ pair:

$$m_{\text{vis}}(D^0) = m(K\ell) = \sqrt{(E_K + E_\ell)^2 - (\vec{p}_K + \vec{p}_\ell)^2}. \tag{3.2}$$

  where $m^2_{K,\ell} = E^2_{K,\ell} - p^2_{K,\ell}$ with m_K and m_ℓ the known masses of the kaon and either the electron or the muon, $m_\mu = 105.658\,\text{MeV}/c$ and $m_e = 510.999\,\text{eV}/c^2$ respectively [32];

- the correccted mass m_{corr} is calculated using invariant mass of the $(D^0\pi^+)$ pair,

calculated without any mass hypotheses on the final state particles:

$$m_{\rm corr}(D^0) = \sqrt{m(K\ell)^2 + p_\perp^2(K\ell)} + p_\perp K\ell), \tag{3.3}$$

it is used to partially account the presence of the neutrino;

- $m(D^0\pi)$ is calculated as:

$$m(D^0\pi) = \sqrt{E^2(K\ell\pi) - p^2(K\ell\pi)}, \tag{3.4}$$

where

$$E(K\ell\pi) = \sqrt{m_{D^0}^2 + p^2(K\ell)} + \sqrt{m_{\pi^+}^2 + p^2(\pi)}, \tag{3.5}$$

$$\vec{p}(K\ell\pi) = \vec{p}(K\ell) + \vec{p}(\pi), \tag{3.6}$$

$$\vec{p}(K\ell) = \vec{p}_{\rm vis} = \vec{p}(K) + \vec{p}(\ell), \tag{3.7}$$

and $m_{D^0} = 1864.84\,\mathrm{MeV}/c^2$ is the known D^0 mass [32]. This variable is similar to $\Delta m = m(K\ell\pi) - m(K\ell)$, *i.e.* the difference between the visible masses of D^{*+} and D^0 respectively. This variable would have a peaking structure around the known value of D^{*+} mass, $m_{D^{*+}} = 2010\,\mathrm{MeV}/c^2$, providing discrimination with respect to the background [55].

Knowing this quantities and the energies and momenta of the charged tracks, it is possible to reconstruct the neutrino momentum. Even if the momentum resolution of the missing neutrino is not comparable with the usual one of a visible track, it is still useful to have such information in order to identify signal events. In the following Section the procedure adopted to estimate the momentum of the missing neutrino will be discussed.

3.2 Analitic reconstruction of the neutrino momentum

A possible way to obtain information on the neutrino is to extract it analitically. The starting point is to compute the invariant mass of the D^0, which is defined as

$$m_{D^0}^2 = (E_{\rm vis} + E_\nu)^2 - (\vec{p}_{\rm vis} + \vec{p}_\nu)^2, \tag{3.8}$$

where, consistently with the definition of m_{vis} given above in Eq. (3.2)

$$\vec{p}_{\text{vis}} = \vec{p}_K + \vec{p}_\ell, \tag{3.9}$$

$$E_{\text{vis}} = E_K + E_\ell. \tag{3.10}$$

Other fundamental variables are the slopes A and B of the conjugation line between the two decay vertices. They are defined as:

$$A \equiv \frac{x_{D^0} - x_{D^*}}{z_{D^0} - z_{D^*}} = \frac{p_K^x + p_\ell^x + p_\nu^x}{p_K^z + p_\ell^z + p_\nu^z}, \tag{3.11}$$

$$B \equiv \frac{y_{D^0} - y_{D^*}}{z_{D^0} - z_{D^*}} = \frac{p_K^y + p_\ell^y + p_\nu^y}{p_K^z + p_\ell^z + p_\nu^z}. \tag{3.12}$$

Substituting the values of Eqs. (3.11) and (3.10), the two slopes become:

$$A = \frac{p_{\text{vis}}^x + p_\nu^x}{p_{\text{vis}}^z + p_\nu^z}, \tag{3.13}$$

$$B = \frac{p_{\text{vis}}^y + p_\nu^y}{p_{\text{vis}}^z + p_\nu^z}. \tag{3.14}$$

At this point, to compute the neutrino momentum, the system written in Eq. (3.15) must be solved:

$$\begin{cases} p_\nu^x = A(p_{\text{vis}}^z + p_\nu^z) - p_{\text{vis}}^x \\ p_\nu^y = B(p_{\text{vis}}^z + p_\nu^z) - p_{\text{vis}}^y \\ m_{D^0}^2 = (E_{\text{vis}} + |\vec{p}_\nu|)^2 - (\vec{p}_{\text{vis}} + \vec{p}_\nu)^2 \end{cases} \tag{3.15}$$

where the neutrino mass is neglected, so as to $E_\nu^2 = p^2$. Introducing the variable t equal to $t = p_{\text{vis}}^z + p_\nu^z$ and substituting the first two lines in the third one obtains Eq. (3.16)

$$E_{\text{vis}}^2 + p_{\text{vis}}^2 - 2t(Ap_{\text{vis}}^x + Bp_{\text{vis}}^y + p_{\text{vis}}^z) + 2E_{\text{vis}}p_\nu = m_{D^0}^2. \tag{3.16}$$

In order to simplify the computing, after isolating p_ν,it is defined the quantity $s = Ap_{\text{vis}}^x + Bp_{\text{vis}}^y + p_{\text{vis}}^z$. Then elevating in quadrature both members, one gets

$$4E_{\text{vis}}^2[(A^2 + B^2 + 1)t^2 - 2ts + p_{\text{vis}}^2] = (m_{D^0}^2 - E_{\text{vis}}^2 - p_{\text{vis}}^2 + 2ts). \tag{3.17}$$

In this way, only the variable t depends on p_ν^z. In order to obtain an equation at second order in t, another ausiliary variable Z is introduced, equal to $Z^2 = m_{D^0}^2 + E_{\text{vis}}^2 - p_{\text{vis}}^2$ and substituting it in the (3.17), we obtain

$$4\left[E_{\text{vis}}^2(A^2 + B^2 + 1) - s^2\right]t^2 - 2\left[2sZ^2\right]t + \left[4E_{\text{vis}}^2 p_{\text{vis}}^2 - Z^4 - 4E_{\text{vis}}^4 + 4Z^2E_{\text{vis}}^2\right] = 0 \tag{3.18}$$

Finally the two solutions for the z-coordinate of the neutrino momentum are obtained:

$$p_\nu^z = \frac{sZ^2 \pm \sqrt{(A^2+B^2+1)(Z^4 - 4m_{D^0}^2 E_{\text{vis}}^2) + 4m_{D^0}^2 s^2}}{2(E_{\text{vis}}^2(A^2+B^2+1) - s^2)} - p_{\text{vis}}^z. \tag{3.19}$$

Once we have the solution of p_ν^z it is possible to compute all the other coordinates, so as to compute the invariant mass of the D^{*+}:

$$m_{D^{*+}} = \sqrt{(E_{\text{vis}} + E_\nu)^2 + (p_{\text{vis}} + p_\nu)^2}\,. \tag{3.20}$$

3.3 Motivations to choose a Global Fit algorithm

In order to compute $R_{\mu/e}$ it is necessary to separate the signal from the background, *i.e.* to have a high precision measurements of the invariant mass of the D^{*+}. Without any information on the neutrino, the invariant mass of the D^{*+} appears in the left side of Fig. 3.2. The invariant mass shown in the figure has been calculated using only the information of the charged tracks

$$m_{\text{vis}}^2(D^*) = m_{\text{vis}}^2 + m_\pi^2 + 2\sqrt{m_{\text{vis}}^2 + p_{\text{vis}}^2}\sqrt{m_\pi^2 + p_\pi^2} - 2\vec{p}_{\text{vis}}\vec{p}_\pi, \tag{3.21}$$

where $m_\pi = 139.57\,\text{MeV}/c^2$, p_{vis} is the total visible D^0 momentum, as defined in Eq. (3.9) and $m_{\text{vis}} = m_{\text{vis}}(D^0)$ is the visible mass of the D^0. Even if a small peak centered around $2.01\,\text{GeV}/c^2$ is visible, the distribution broadens through the whole invariant mass interval shown. Also on the right side of Fig. 3.2, the D^{*+} invariant mass is represented, in this case it is calculated using the true momentum of the neutrino (see Sec. 2.6) and a narrow peak, in correspondance of $2.01\,\text{GeV}/c^2$, is visible. In Fig. 3.2 the distribution shown are obtained with simulated events. As a result, in order to obtain the highest precision measurements, it is necessary to find a suitable way to evaluate the neutrino momentum.

Using the analitical resolution to calculate neutrino momentum shows the problem that sometimes there are no real solutions, since the parameters may bring to a negative discriminant in the Eq. (3.19), due to the momentum resolution of the visible tracks.

The implementation of a GF algorithm, would address these issue. The key point of the GF algorithm is to write a single function of a set of parameters which describes the whole decay chain and gets minimised in order to obtain the values of the parameters which better fit to the measured data. The chosen statistical approach is the least squares method. The output of the GF comprehends all the parameters describing the decay, including the neutrino's momentum vector. Thanks to the GF, it is possible to compute the D^{*+} invariant mass and to evaluate the q^2, fundamental for the analysis of $R_{\mu/e}(q^2)$.

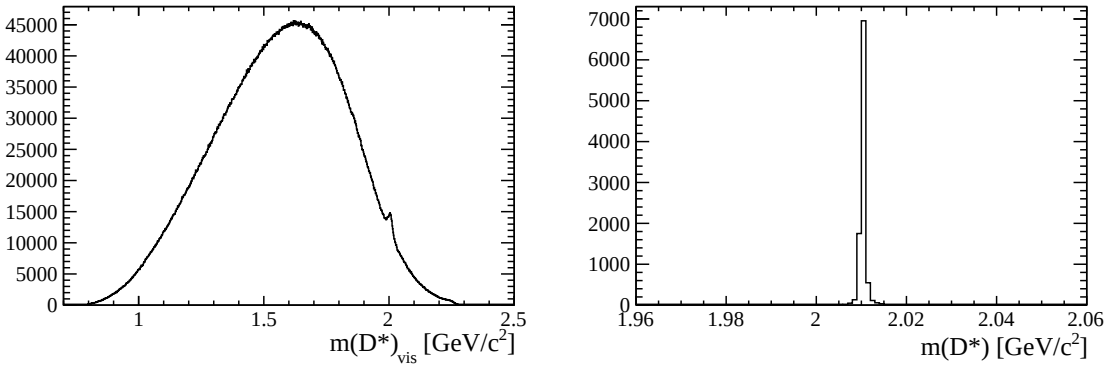

Figure 3.2: Left: the visible mass of the D^*, which is m_{D^*} calculated without any information on the neutrino, as if the decay was $D^{*+} \to D^0(\to K^-\ell^+)\pi^+$. Right: Invariant mass of the D^{*+} computed using the MC truth.

3.3.1 The least squares method

In many situations, as in high energy physics, a measured value y can be considered as a Gaussian random variable centered on the quantity's true value ϕ. Following the central limit theorem, this is valid as long as the total error is the sum of small contributions. Let's consider an set of N variables y_i, Gaussian-distributed with a known covariance matrix V, but unknown mean values, and related to x_i, which is assumed to be known with precision. Supposing that the true value is given as a function of x, $\phi(\vec{x};\, \vec{\theta})$, where $\vec{\theta} = (\theta_1, \ldots, \theta_m)$ are unknown parameters, the method of the least square (LS) aims to estimate these parameters, given the data $x_1, \ldots, x_n$. It also gives the possibility to evaluate the goodness-of-fit of the hypothesised function $\phi(z;\, \vec{\theta})$.

The core idea of the LS method is finding the values of $\vec{\theta}$ which minimise the quantity:

$$\chi^2(\vec{\theta}) = \sum_{i=1}^{N} \Big(y_i - \phi(x_i;\, \vec{\theta})\Big)\, (V^{-1})_{ij}\, \Big(y_j - \phi(x_j;\, \vec{\theta})\Big)\,. \tag{3.22}$$

If $\phi(\vec{x};\, \vec{\theta})$ is a linear function of the parameters, as

$$\phi(\vec{x};\, \vec{\theta}) = \sum_{j=1}^{m} a_j(\vec{x})\theta_j = \sum_{j=1}^{m} A_{ij}\theta_j, \tag{3.23}$$

where $A_{ij} = a_j(\vec{x})$, Eq. (3.22) becomes

$$\chi^2 = (\vec{y} - \vec{\phi})^T V^{-1} (\vec{y} - \vec{\phi}) \tag{3.24}$$

$$= (\vec{y} - A\vec{\theta})^T V^{-1} (\vec{y} - A\vec{\theta}), \tag{3.25}$$

where $\vec{y} = (y_1,\ \ldots,\ y_N)$ is the vector of the measured values and $\vec{\phi} = (\phi_1,\ \ldots,\ \phi_N)$ contains

the predicted values $\phi_i = \phi(x_i; \vec{\theta})$. In order to find the minimum χ^2, the first derivative of θ_i must be set to zero

$$\nabla\chi^2 = -2(A^T V^{-1}\vec{y} - A^T V^{-1} A\vec{\theta}) = 0. \tag{3.26}$$

This can be solved for estimators $\hat{\vec{\theta}}$, providing that $A^T V^{-1} A$ is not singular

$$\hat{\vec{\theta}} = (A^T V^{-1} A)^{-1} A^T V^{-1}\vec{y} \equiv B\vec{y}. \tag{3.27}$$

As a consequence, the parameters $\vec{\theta}$ are a linear function of the original measurements. In order to find the covariance matrix for the estimators $U_{ij} = \mathrm{cov}[\theta_i, \theta_j]$, error propagation is used and it gives

$$C = BVB^T = (A^T V^{-1} A)^{-1}. \tag{3.28}$$

Considering this, it is possible to write the χ^2 as

$$\chi^2 = (\vec{y} - \hat{\vec{\theta}})C^{-1}(\vec{y} - \hat{\vec{\theta}})^T, \tag{3.29}$$

where θ is the physical quantity, $\vec{\theta} = \hat{\vec{\theta}}C$ is the measured one and C^{-1} is the covariance matrix of the two quantities. Since the kinematic of the decay comprehends a large number of constraints, a χ^2 must be computed for each of them. Thanks to the linearity of the χ^2, the final χ^2 is a sum all of these.

3.4 Global Fit strategy

In Sec. 2.3.5 the parametrisation of the charged tracks after the reconstruction has been shown. For every $z = z_{\mathrm{Ref}}$ π, K and ℓ tracks are parametrised as

$$\vec{\alpha} = \left(x,\, y,\, t_x,\, t_y,\, \frac{q}{|\vec{p}|}\right)_{z_{\mathrm{Ref}}} \tag{3.30}$$

where q is the charge of the particle, $|\vec{p}|$ is the total particle momentum and t_x and t_y are the two slopes:

$$t_x = \frac{dx}{dz} = \frac{p_x}{p_z}, \tag{3.31}$$

$$t_y = \frac{dy}{dz} = \frac{p_y}{p_z}, \tag{3.32}$$

where p_i is the i-th coordinate of the momentum. The measured quantities are the tracks of the charged particles, π, K and ℓ (μ or e), the position of the D^0 decay vertex and the

coordinates of the primary vertex. For each track the χ^2 is calculated as follows

$$\chi^2_K = (\vec{\alpha}_K - \hat{\vec{\alpha}}_K)C_K^{-1}(\vec{\alpha}_K - \hat{\vec{\alpha}}_K)^T, \tag{3.33}$$

$$\chi^2_\ell = (\vec{\alpha}_\ell - \hat{\vec{\alpha}}_\ell)C_\ell^{-1}(\vec{\alpha}_\ell - \hat{\vec{\alpha}}_\ell)^T, \tag{3.34}$$

$$\chi^2_\pi = (\vec{\alpha}_\pi - \hat{\vec{\alpha}}_\pi)C_\pi^{-1}(\vec{\alpha}_\pi - \hat{\vec{\alpha}}_\pi)^T, \tag{3.35}$$

$$\chi^2_{\mathrm{PV}} = (\vec{\alpha}_{\mathrm{PV}} - \hat{\vec{\alpha}}_{\mathrm{PV}})C_{\mathrm{PV}}^{-1}(\vec{\alpha}_{\mathrm{PV}} - \hat{\vec{\alpha}}_{\mathrm{PV}})^T, \tag{3.36}$$

where α_i is the physical quantity, $\vec{\alpha_i} = \hat{\vec{\alpha_i}}C$ is the measured one and C^{-1} is the covariance matrix of the two quantities. Due to the logarithmic nature of the χ^2, the final function to be minimised will be the sum of all these chi-square functions and the one related to the constraint of the invariant mass, which are explained in detail in the next section. The function is

$$f(\vec{\theta}, \hat{\vec{\theta}}) = \chi^2_{\mathrm{PV}} + \chi^2_\pi + \chi^2_\ell + \chi^2_K + \chi^2_{D^0}, \tag{3.37}$$

where $\hat{\vec{\theta}}$ is the vector of the parameters to be estimated from the minimisation.

3.4.1 Implementation of the constraints

In order to compute the GF it is necessary to keep in mind the kinematic of the $D^{*+} \to D^0\ (\to K^-\ell^+\nu_\ell)\pi^+$ decay, represented in Fig. 3.1. As above said, the D^{*+} instantaneously decays in $D^{*+} \to D^0\pi^+$, so the first decay vertex corresponds to the pp interaction vertex (primary vertex, PV). As a consequence, the π track must point to the PV. On the other hand, the secondary vertex of the D^0 decay is displaced from the PV, it is identified as the interaction point of the two charged daughter tracks (K^- and ℓ^+). Moreover, the invariant mass of the D^0, must be equal to the known value of $m_{D^0} = 1864.83\,\mathrm{MeV}/c^2$ [32]. All things considered, five constraints must be computed as follows:

Invariant mass of the D^0 The first kinematical constraint is the invariant mass of the D^0. Starting from (3.8), and developing it, m_{D^0} is obtained by

$$m^2_{D^0} = m^2_K + m^2_\ell + 2\sqrt{m^2_K + p^2_K}\sqrt{m^2_\ell + p^2_\ell} + 2p_\nu\sqrt{m^2_\ell + p^2_\ell} + 2p_\nu\sqrt{m^2_K + p^2_K} + \\ - 2\vec{p}_K\vec{p}_\nu - 2\vec{p}_\ell\vec{p}_\nu - 2\vec{p}_\ell\vec{p}_K \tag{3.38}$$

where all the masses values (m_ℓ, m_K) are taken from the Particle Data Group's latest review [32]. The computed invariant mass is gaussian constrained to the value from the PDG, so the following χ^2 is written:

$$\chi^2_{D^0} = \frac{(m_{D^0} - \hat{m}_{D^0})^2}{2\sigma^2_{m_{D^0}}} \tag{3.39}$$

where $\sigma^2_{m_{D^0}} = 0.001\,\text{GeV}/c^2$, greater than the PDG value, which is $5 \times 10^{-5}\,\text{GeV}/c^2$, but small enough to constraint at the level of few MeV/c^2 the D^0 invariant mass;

D^0 secondary vertex The two tracks of the charged daughters (ℓ and K) of the D^0 have to come from the same vertex. In order to get a constraint from this, the first two coordinates of the track (x and y) must be reparametrised using the vertex coordinates as follows

$$\begin{cases} \hat{x}^{K/\ell} = x_{D^0} + (z_{\text{Ref}} - z_{D^0})\hat{t}_x^{K/\ell} \\ \hat{y}^{K/\ell} = y_{D^0} + (z_{\text{Ref}} - z_{D^0})\hat{t}_y^{K/\ell} \end{cases} \tag{3.40}$$

where $\hat{t}_i^{K/\ell}$, for $i = x, y$, is the ratio between the i-th coordinate of the K or ℓ momentum and the z one. The chi-square is then calculated as in Eq. (3.33) and (3.34);

D^{*+} corresponds to the primary vertex In order to exploit the fact that the D^0 comes from the primary vertex, a similar reparametrisation as previously described has been adopted

$$\begin{cases} \hat{x}_{\text{PV}} = x_{D^0} + (z_{\text{PV}} - z_{D^0})\hat{t}_x^{D^0} \\ \hat{y}_{\text{PV}} = y_{D^0} + (z_{\text{PV}} - z_{D^0})\hat{t}_y^{D^0} \end{cases} \tag{3.41}$$

where, the momentum of the D^0 is calculated as $\vec{p}^K + \vec{p}^\ell$, and $\hat{t}_x^{D^0}$ and $\hat{t}_y^{D^0}$ are

$$\hat{t}_x^{D^0} = \frac{\hat{p}_x^K + \hat{p}_x^\ell + \hat{p}_x^\nu}{\hat{p}_z^K + \hat{p}_z^\ell + \hat{p}_z^\nu}, \tag{3.42}$$

$$\hat{t}_y^{D^0} = \frac{\hat{p}_y^K + \hat{p}_y^\ell + \hat{p}_y^\nu}{\hat{p}_z^K + \hat{p}_z^\ell + \hat{p}_z^\nu}. \tag{3.43}$$

The relative chi-square is in Eq. (3.36).

Pion coming from the primary vertex It is related to the $D^* \to D^0\pi^+$ decay. Similarly to the charged tracks of the kaon and the lepton, it is parametrised as follows

$$\begin{cases} \hat{x}_\pi = x_{\text{PV}} + (z_{\text{Ref}} - z_{\text{PV}})\hat{t}_x \\ \hat{y}_\pi = y_{\text{PV}} + (z_{\text{Ref}} - z_{\text{PV}})\hat{t}_y \end{cases} . \tag{3.44}$$

Its χ^2 is expressed in Eq. (3.35).

3.4.2 Minimisation

Finally, the function to minimise is the sum of all the single contributions:

$$f(\vec{\theta}, \hat{\vec{\theta}}) = \chi^2_{\rm PV} + \chi^2_{\pi} + \chi^2_{\ell} + \chi^2_{K} + \chi^2_{D^0}, \tag{3.45}$$

where $\hat{\vec{\theta}}$ is the vector of the parameters which will be estimated and it includes:

- $\vec{p}_\nu$, the coordinates of the neutrino momentum;
- $\vec{p}_\ell$, the coordinates of the momentum of the lepton (electron or muon);
- $\vec{p}_K$, the coordinates of the kaon momentum;
- $\vec{p}_\pi$, the coordinates of the momentum of the soft pion;
- $\vec{x}_{D^0}$, the position of the D^0,
- the third coordinate of the primary vertex $z_{\rm PV}$.

In summary, in the minimisation of Eq. 3.45 there are 16 free parameters, starting from 18 measured quantities, *i.e.* tracks' measurements and the mass values.

3.5 Implementation of the algorithm

The GF algorithm is implemented using members of the `TMinuit` class of the ROOT Data Analysis Framework. In order to use MINUIT directly, it is necessary to wrap the final chi-square of Eq. 3.45, in a way it can be processed. In fact, MINUIT call a void function with specific arguments: `(int& nDim, double* gout, double& result, double par[], int flag)`, where `par[]` is the array of the parameters and the variable `result` must be equal to the value of the function which has to be minimised. The MIGRAD algorithm has the task to compute the first derivative, so after setting the parameters value, it is called. Each time, the information on the value of the function, the precision of the fit, name EDM, and the status (converged or not) is saved. If MIGRAD does not fulfil the requirements, such as converged status and EDM below 10^{-3} (actually this value can be opportunely tuned), it is called again, until the fit converges with the desired EDM.

Due to the instantaneous luminosity in the LHCb interaction point, an average of about 2 pp collisions can occur per bunch crossing. A strategy to choose a primary vertex is implemented. Moreover, the value of $\vec{p}_\nu$ is unknown. Also in this case a method to set the initial value of is foreseen through a nested algorithm: the values of p^x_ν and p^y_ν are set to 0 GeV/c (in general in LHCb the p_x and p_y value of a track is small), while the value of, p^z_ν is chosen between ten different values, such as (0, 5, 10, 15, 20, 35, 40, 60, 80, 100) GeV/c,

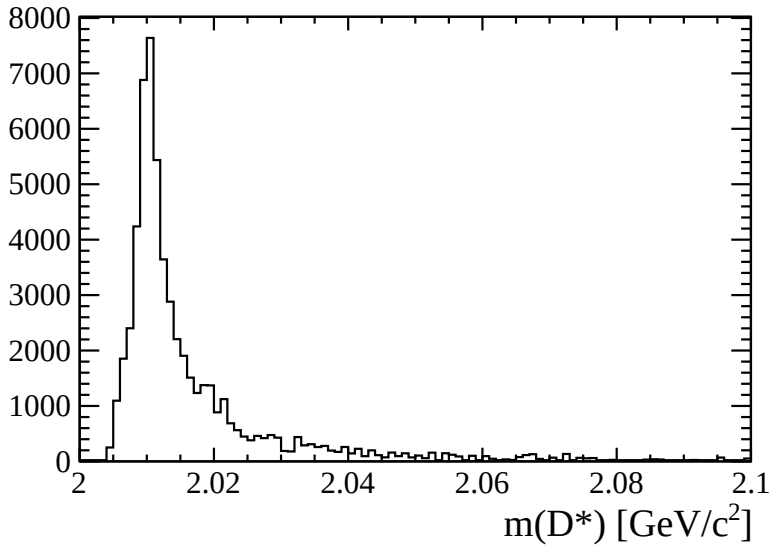

Figure 3.3: D^{*+} invariant mass computed using the Global Fit output on the MC sample. The events correspond to $D^{*+} \to D^0\ (K^-\mu^+\nu_\mu)\pi^+$ decay.

corresponding to different starting point of several minimisations of the χ^2 function. The value of the initial p_z corresponding to the best χ^2 is choosen as the default starting point for each event. This procedure is adopted to avoid the convergence of the function to local minima. The function is then minimised for each measured primary vertex ($x_{\rm PV}$, $y_{\rm PV}$, $z_{\rm PV}$) and the value of the parameters corresponding to the best χ^2 is chosen as final result.

3.6 Global Fit performances

Before applying this procedure to the data, the GF algorithm has been tested on the $D^{*+} \to D^0\ (K^-\mu^+\nu_\mu)\pi^+$ MC data sample. In Figs. 3.3 and 3.4 the invariant mass of the D^{*+} and the visible mass of the D^0 are represented respectively. They have been computed using the global fit, applied on a sample with about 50000 MC events (see Ch. 4). In Fig. 3.3, the invariant mass distribution shows a clear peak in correspondance of the value of the D^*, $2.010\,\mathrm{GeV}/c^2$, as expected, with a small tail. Comparing this distribution with the one shown in Fig. 3.2, it is evident how the GF performs, even if the invariant mass resolution on the D^{*+} is larger than a typical one of a fully reconstructed decay.

The invariant mass distribution for the same variables for both electron and muon channels of $m(D^*)$ and $m_{\mathrm{vis}(D^0)}$ computed using the GF on the data set collected by LHCb during the 2015 data taking campaign are shown in Figs. 3.5 and 3.6 respectively. Both D^{*+} invariant mass plots show a recognisable peak at about $2.01\,\mathrm{GeV}/c^2$, as expected.

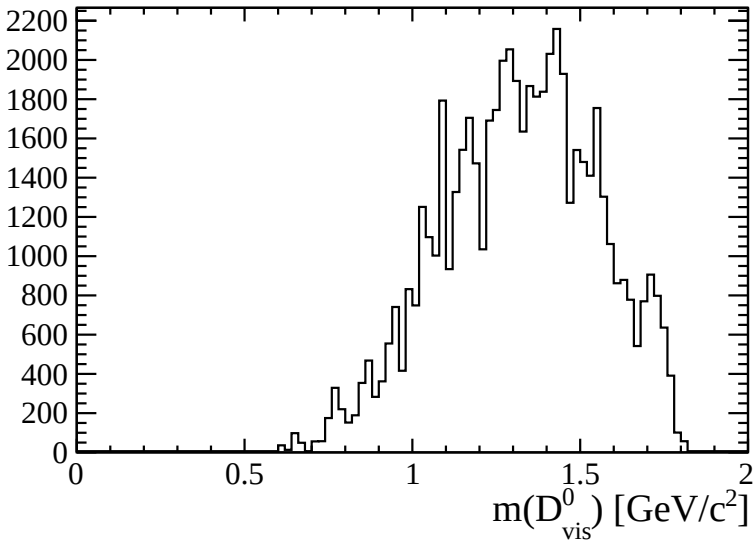

Figure 3.4: D^0 visible mass computed using the Global Fit output on the MC sample. The events correspond to $D^{*+} \to D^0\ (K^-\mu^+\nu_\mu)\pi^+$ decay.

The tail of the plot is mainly due to the combinatorial background, even if a log signal tail is present.

The D^0 visible mass invariant mass distribution ashow different shape and peaks between the two different decay modes. In the case of electron final state (e-channel) is evident the precence of different sources of background (see Sec. 4.2). The highest peak of the e-channel distribution, also present in the μ-channel, at a $m_{\rm vis}(D^0)$ of about $1.8\,\mathrm{GeV}/c^2$ corresponds to the D^0 decay $D^0 \to K^-\pi^+$, where a charged pion is mis-identified as either a muon or an electron. The different height in the two spectra are due to the different efficiency in the mis-identification of the two leptons. Fig. 3.5 also show a different signal yields as well as a different invariant mass resolution. The muons generate hits in almost all subdetectors (long and downstream tracks), while the electrons generate hits in fewer parts of the detector: the VELO, the tracking stations and the ECAL. Moreover, due to its interaction with the materials, *i.e.* generation of electromagnetic showers, the electron tracks is more difficult to reconstruct. The reconstruction efficiency of the electron, in fact, is one of the many challenges of this analysis. In addition, due to bremsstrahlung radiation dominant in the e-channel, the momentum of the electron is measured with less precision than the muon one, with the consequence of a worse invariant mass resolution.

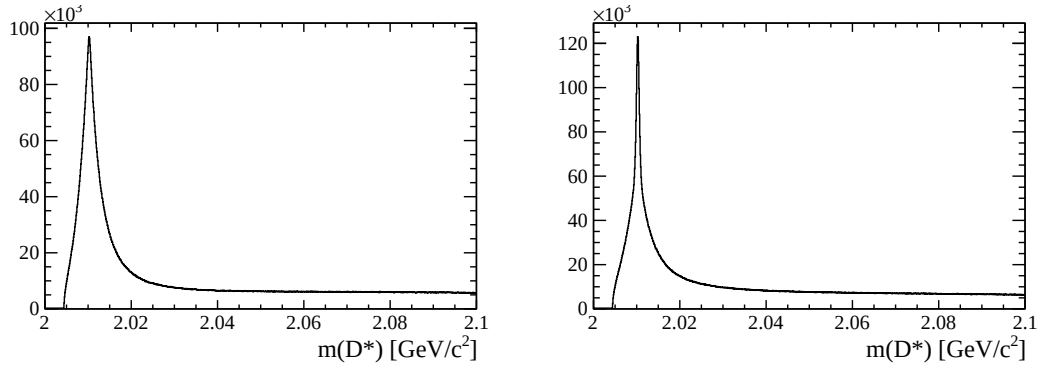

Figure 3.5: D^{*+} invariant mass computed using the Global Fit on the 2015 data-set for both lepton flavours e and μ.

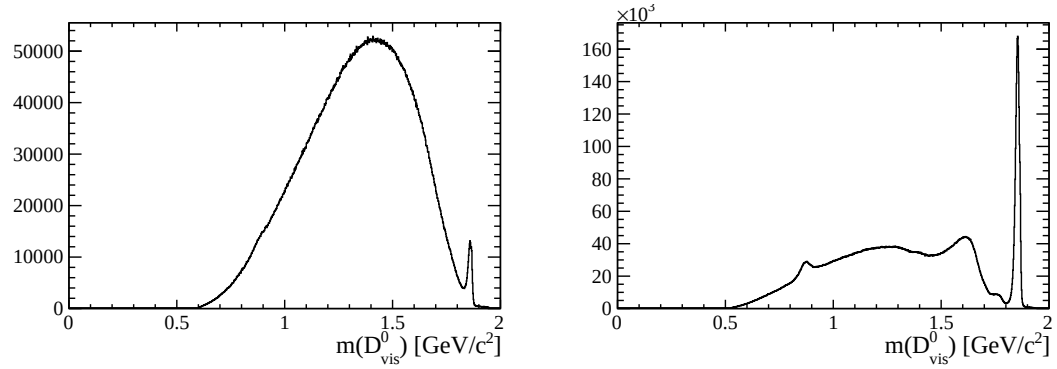

Figure 3.6: D^0 visible mass ccomputed using the Global Fit on the 2015 data-set for both lepton flavours e and μ.

Chapter 4

Signal Yields

In order to extract the signal yields from data it is necessary to know how the background is composed and how much it interferes with the real signal. In Sec. 4.1 the combinatorial background and its modeling in the fit model is discussed. In Sec. 4.2, partially reconstructed background, with a decay topology similar to the signal are studied. A study of the momentum imbalance between the decay products is performed in order to identify possible sources of such backgrounds and apply proper PID requirements.

4.1 Combinatorial background hypothesis

The combinatorial background consists in one or more particles (especially pions) coming from other processes are wrongly associated with the reconstructed D^0 decay. The effect of this background is the introduction of a long tail in the $m(D^*)$ distribution.

In order to extract the signal yield, an extended chi-square fit of the D^{*+} mass, computed after the global fit, is used. The signal is modelised as a sum of three probability density functions (PDF):

$$f(m) = \alpha_2 \left(\alpha_1 G_1(m;\mu_1,\sigma_1) + \alpha_2 G_2(m;\mu_2,\sigma_2)\right) + \alpha_2 J(m;\mu_j,\sigma_j,\delta_j,\gamma_j) \tag{4.1}$$

where α_1 and α_2 are free parameters with a value between 0 and 1, $G_1(m;\mu_1,\sigma_1)$ and $G_2(m;\mu_2,\sigma_2)$ are two gaussian PDF and $J(m;\mu_j,\sigma_j,\delta_j,\gamma_j)$ is a Johnson function [56]. The background is described by the following PDF

$$f(m;\mu,\beta,\xi) = (m - m_{\min})^{\beta} e^{-\xi(m-m_{\min})}, \tag{4.2}$$

where m is the D^{*+} mass, $m_{\min}$ is the minimum value of the variable m, and β and ξ are free parameters.

The D^{*+} invariant mass distribution with the result of the fit overlaid is shown in Fig. 4.1 and 4.2 for both muon and electron decay modes. The data are represented by

Table 4.1: Results of the fit. The number of signal events is not reported because the analysis is still ongoing (blind).

Quantity	$K^-e^+\nu_e$ mode	$K^-\mu^+\nu_\mu$ mode
N_{BKG}	(1571926 ± 27143)	(3478388 ± 15211)
$\mu_1(\,\mathrm{GeV}/c^2)$	(2.004 ± 0.016)	(2.014700 ± 0.000058)
$\mu_2(\,\mathrm{GeV}/c^2)$	(2.004000 ± 0.000004)	(2.010400 ± 0.000010)
$\mu_j(\,\mathrm{GeV}/c^2)$	$(2.0102973 \pm 0.0000043)$	$(2.0102000 \pm 0.0000034)$
$\sigma_1(\,\mathrm{GeV}/c^2)$	(1.00 ± 0.98)	$(4.30 \pm 0.04) \times 10^{-3}$
$\sigma_2(\,\mathrm{GeV}/c^2)$	$(0.603 \pm 0.012) \times 10^{-3}$	$(2.27 \pm 0.01) \times 10^{-3}$
$\sigma_j(\,\mathrm{GeV}/c^2)$	(1.580 ± 0.005)	$(0.884 \pm 0.008) \times 10^{-3}$

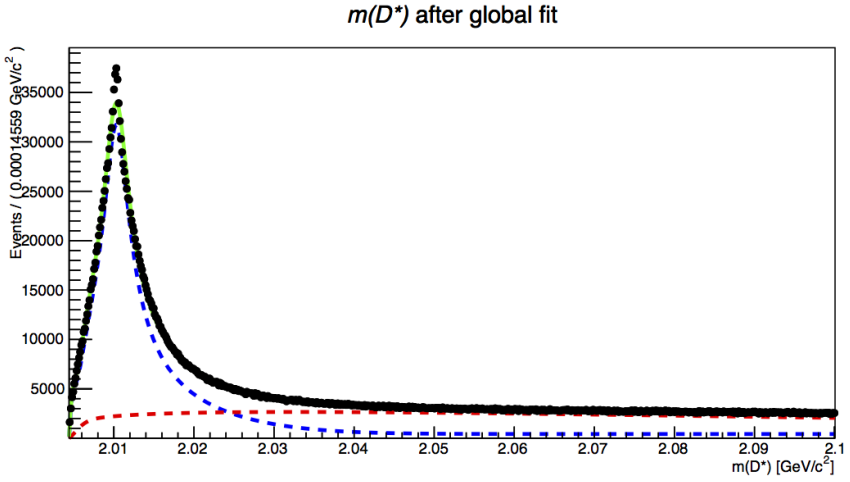

Figure 4.1: Distribution of the D^{*+} invariant mass with the result of the fit overlaid for the electron decay mode. The data are processed with the GF algorithm.

black points with the error bars, while the signal component is in blue and the background in red. In Table 4.1 the quantities calculated by the fit are represented. In this fit, the physical background is not yet considered. In the following section a preliminary study is performed in order to quantify how many events for each potential background can be present in the invariant mass spectrum, in particular under the D^* peak.

4.2 Background evaluation

The main physical backgrounds of the $D^0 \to K\ell\nu_\ell$ decay are due to misreconstructed D^0 decays, like $D^0 \to \pi^-\mu^+\nu_\mu$ and $D^0 \to \pi^-e^+\nu_e$, where a pion is misidentified as a kaon or a lepton, and partially reconstructed D^0 decays, like $D^0 \to K^-\mu^+\nu_\mu\pi^0$ (resonant and non-resonant).

In order to evaluate the potential dangerousness of these shapes of the backgrounds,

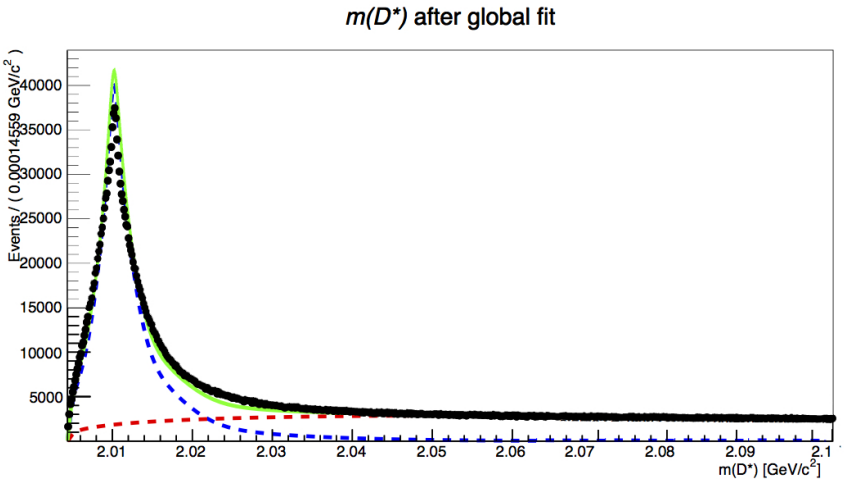

Figure 4.2: Distribution of the D^{*+} invariant mass with the result of the fit overlaid for the muon decay mode. The data are processed with the GF algorithm.

the invariant mass spectra of three different background decay channels were analysed using MC. In Fig. 4.3 the variables $m(D^*)$ and $m_{vis}(D^0)$ computed with the output of the GF, each background hypotheses and for the signal decay with a muon in the final state, are represented.

It is possible to recognise different main background final states for each decay mode:

- The background final states of the muon mode comprehend:
  - the $K^- e^+ \nu_e$ final state where an electron is mis-identified as a muon,
  - the $\pi^- \mu^+ \nu_\mu$ final state, where a pion is mis-identified as a kaon,
  - the partially reconstructed D^0 decays, with the resonant $K^{*\,-} \mu^+ \nu_\mu$ final state and the not resonant one, $K^- \mu^+ \nu_\mu \pi^0$;
- In analogy with the muon mode, the background of the electron decay mode are:
  - the $K^- \mu^+ \nu_\mu$ final state where an electron is mis-identified as a muon,
  - the $\pi^- e^+ \nu_e$ final state, where a pion is mis-identified as a kaon,
  - the partially reconstructed D^0 decays: the resonant $K^{*\,-} e^+ \nu_e$ final state and the not resonant $K^- e^+ \nu_e \pi^0$;
- The background final states shared by the two decay modes comprehends the final states where the pion is mis-identified as either a muon or a lepton, such as the $K^- \pi^+ \pi^0$ final state and the $\pi^+ \pi^- \pi^0$ final states, where another π is mis-identified as a K. In particular, it is possible to note that in Fig. 4.3 the D^0 invariant mass distribution for the $K^- \pi^+ \pi^0$ final state has a shape similar to the distribution for the $K^- \mu^+ \nu_\mu$ final state.

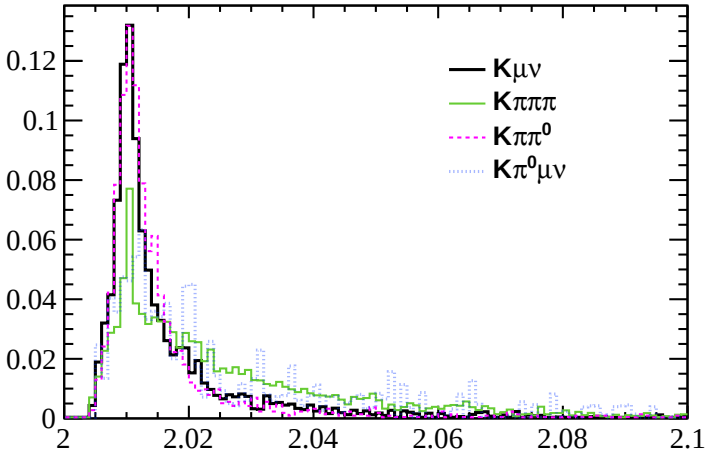

(a)

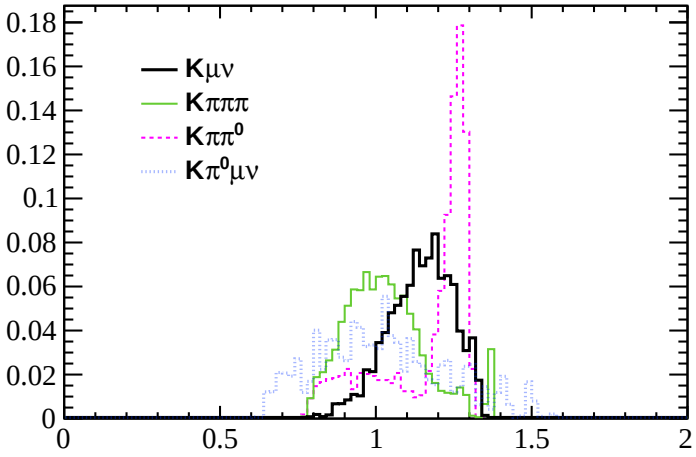

(b)

Figure 4.3: D^{*+} invariant mass and D^0 visible mass distribution, with different final states for the muon decay mode: $K^-\mu^+\nu_\mu$ (black), K^- 3π (green), $K^-\pi^+\pi^0$ (magenta) and $K^-\pi^0\mu^+\nu_\mu$ (light violet). The MC data are processed with the GF algorithm.

The decay channels with a netrual pion in the final state can be avoided with efficienct reconstruction and particle ID of the final state, in addition to constrain the invariant mass of the D^0 (3.8). In fact, the neutrino mass is approximated to zero, while $m_{\pi^0} = 134.977\,\mathrm{MeV}/c^2$ [32]. These decay channels and their branching fractions ($\mathcal{B}$) are summarized in Table 4.2.

Table 4.2: Signal and major backgrounds of the $D^0 \to K\ell\nu_\ell$ analysis and respective branching fractions.

$D^0 \to$	Branching fraction [32]
$K^-\mu^+\nu_\mu$	$(3.33 \pm 0.13)\%$
$K^-e^+\nu_e$	$(3.538 \pm 0.033)\%$
$\pi^+\pi^-\pi^0$	$(1.47 \pm 0.09)\%$
$K^{*\,-}e^+\nu_e$	$(2.16 \pm 0.16)\%$
$K^{*\,-}\mu^+\nu_\mu$	$(1.92 \pm 0.25)\%$
$K^-\pi^0e^+\nu_e$	$(1.6\ ^{+1.3}_{-0.5})\%$
$K^-\pi^0\mu^+\nu_\mu$	$< 0.14\%$
$\pi^-e^+\nu_e$	$(0.291 \pm 0.004)\%$
$\pi^-\mu^+\nu_\mu$	$(0.238 \pm 0.024)\%$
$K^-\pi^+\pi^0$	$(1.14\ ^{+0.50}_{-0.21})\%$

4.2.1 Momenta asymmetry

A method to visualise the various physical background is to study the $m(D^*)$ and $m_{vis}(D^0)$ distributions as a function of the asymmetry of the momentum of the final states, defined as

$$A_p = \frac{p_\ell - p_K}{p_\ell + p_K}, \tag{4.3}$$

the signal is visible as vertical regions, while background decay channels have a curved region. For further comprehension, it is useful to compare these plots to their projection on the x-axis, as shown as swhon in the bottom part of the plots.

In Figs. 4.5 and 4.7 are reported the distribution of $m(D^*)$ and $m_{\rm vis}(D^0)$ as a function of A_p, where it is evident, comparing these distributions with the one on Figs. 4.4 and 4.6 that the physical background is highly reduced.

The most visible structure is the peak in the invariant mass distribution of $m_{vis}(D^0)$, placed at about $1.8\,\mathrm{GeV}/c^2$ in Fig. 4.4 for $-0.8 < A_p < 0.8$. The same peak is also visible in the in the bottom left part of the Figure and it can be attributed to $D^0 \to K^-K^+$ decay. The other visible peaks are one at about $m_{vis}(D^0) = 1.6\,\mathrm{GeV}/c^2$, and the other at abot $0.9\,\mathrm{GeV}/c^2$. These can be attributed to the $D^0 \to K^-\pi^+\pi$ and the $D^0 \to \pi^-\pi^+$ decays, respectively.

In order to reduce the physical background components PID requirement are applied. In particular, the PID requirements for the two decays respectively are:

- PID for the kaon: `ProbNNk`> 0.9,
- PID for the electron: `ProbNNe`> 0.6 `&& ProbNNk`< 0.1,
- PID for the muon: `ProbNNmu`> 0.6 `&& l_ProbNNk`< 0.1.

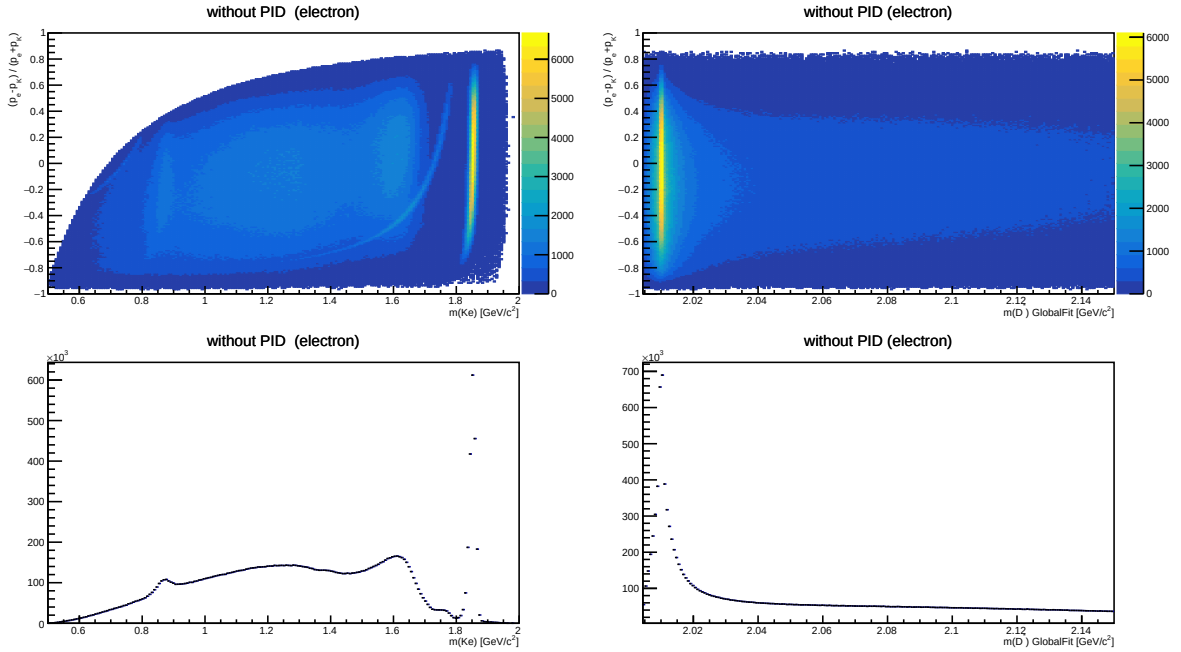

Figure 4.4: D^0 and D^{*+} Mass vs asymmetry of momenta, before PID cuts.

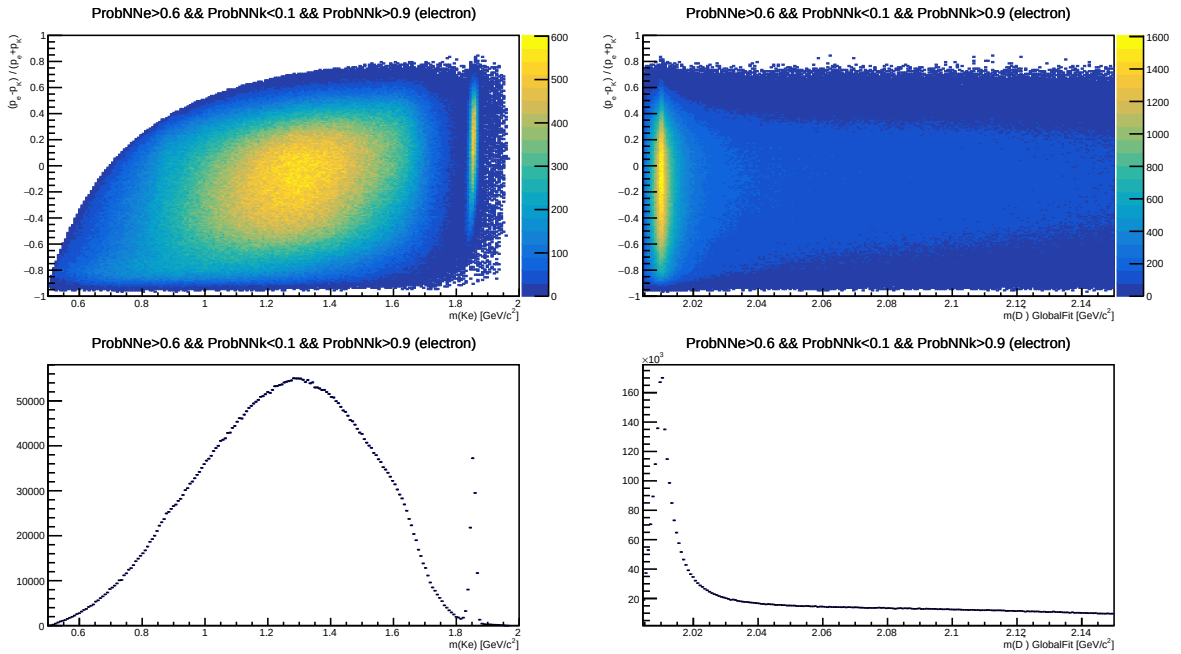

Figure 4.5: D^0 and D^{*+} Mass vs asymmetry of momenta, after PID cuts.

After the PID cuts, in Fig. 4.5, the effectiveness of the PID requirements is evident. The the D^0 visibile mass has a shape similar to the one computed using the MC data (Fig. 4.3(b)).

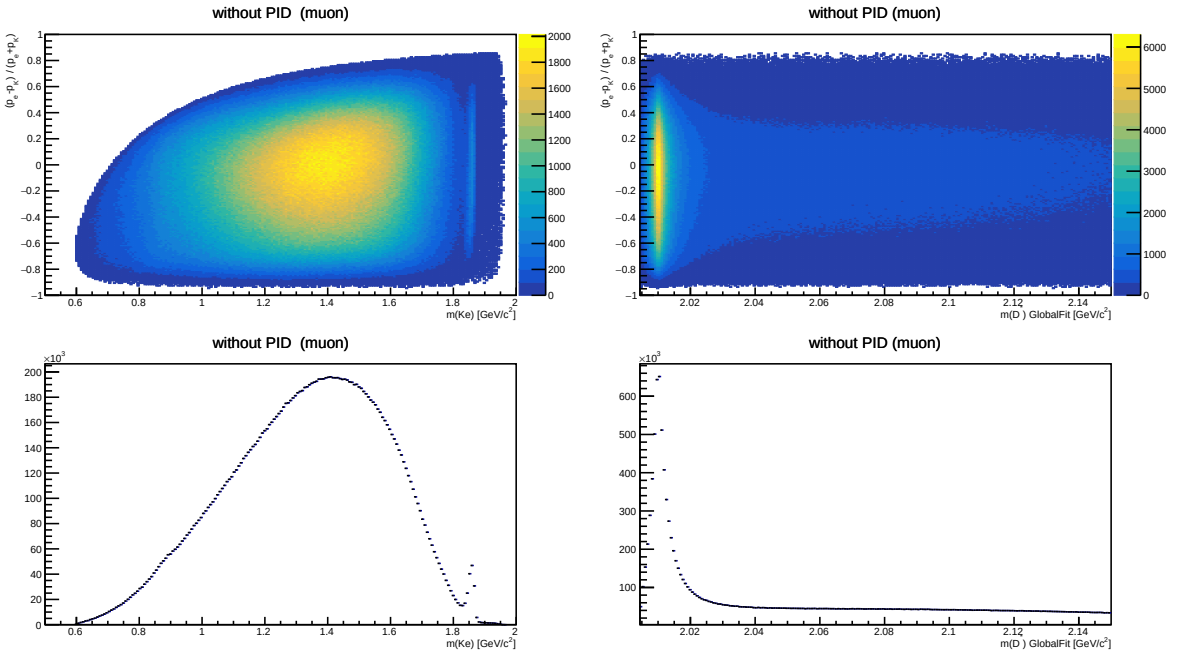

Figure 4.6: D^0 and D^{*+} Mass vs asymmetry of momenta, before PID cuts.

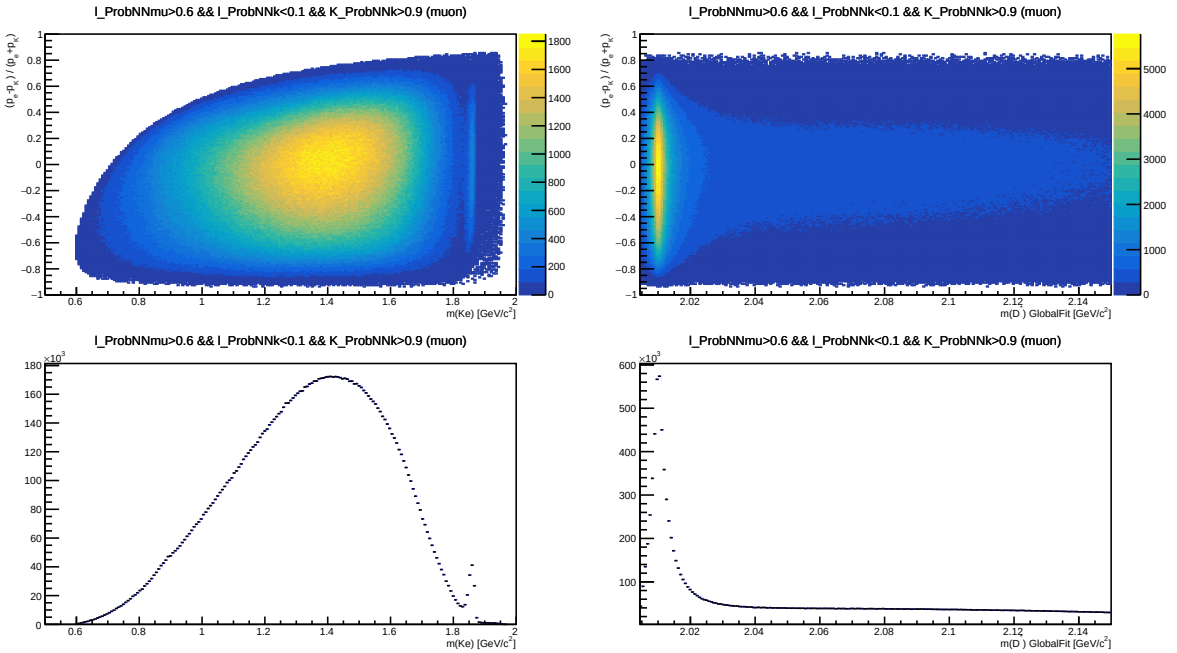

Figure 4.7: D^0 and D^{*+} Mass vs asymmetry of momenta, after PID cuts.

Table 4.3: List of the different decay channels after the stripping and the branching fractions used in the analysis.

Name	EvtType	$\mathcal{B}[\%]$
$D^0 \to K\mu\nu_\mu$	27173001	3.31
$D^0 \to Ke\nu_e$	27583002	3.55
$D^0 \to KK$	27163002	0.396
$D^0 \to \pi\pi\pi^0$	27163403	1.43
$D^0 \to K\pi\pi^0$	27263400	14.3
$D^0 \to K\ 3\pi$	27265000	8.08
$D^0 \to K^*\mu\nu_\mu$	27572001	1.91
$D^0 \to \pi\mu\nu_\mu$	27573001	0.289
$D^0 \to \mu\nu_\mu\pi^0$	27573400	1.91
$D^0 \to K^*e\nu_e$	27582401	2.16
$D^0 \to \pi e\nu_e$	27583000	0.237
$D^0 \to e\nu_\mu\pi^0$	27583400	1.6

4.2.2 Evaluation of the background from the number of events

The numbers of physical background events that passed the full selection, including the PID requirements, are evaluated using MC events and calculated using the expression

$$\left(\frac{N_{BKG}}{N_{SIG}}\right)_i = \frac{(\mathcal{B}_i \cdot \epsilon_{\text{GEN}} \cdot \epsilon_{\text{sel}})_i}{(\mathcal{B}_{SIG} \cdot \epsilon_{\text{GEN,SIG}} \cdot \epsilon_{\text{sel}})_{SIG}}, \tag{4.4}$$

where ϵ_{GEN} is the efficiency of the generator level requirements used in the simulation to minimise the computation time, $\mathcal{B}_i$ is the branching ratio of the i-th background component and ϵ_{sel} is the offline selection efficiency, including the PID requirements. The various sources of background analysed are reported In Table 4.3, together with the branching fraction and the EvtGen code, which identified unequivocally the decay in the simulation software, are shown. The values of $\frac{N_{BKG}}{N_{SIG}}$ together with the various efficiencies are reported in Tables 4.4 and 4.5.

Table 4.4: Values of the different efficiencies for each decay channel for the signal decay with the e in the final state.

Final state	$\mathcal{B}_i$ (%)	ϵ_{GEN} (%)	ϵ_{sel} (%)	$\frac{N_{BKG}}{N_{SIG}}$ (%)
$Ke\nu_e$	3.55	21.91	0.26	100
KK	0.40	22.88	2.83×10^{-5}	1.2×10^{-3}
$K\pi\pi\pi^0$	1.43	20.00	0	0
$K\mu\nu_\mu$	3.31	22.44	8.55×10^{-5}	0.03
$K\pi\pi^0$	14.3	19.27	7.70×10^{-4}	1.07
$K3\pi$	8.08	20.00	1.43×10^{-4}	0.12
$K^*\mu\nu_\mu$	1.86	19.68	0	0
$\pi\mu\nu_\mu$	0.29	21.30	0	0
$K\mu\nu_\mu\pi^0$	1.38	19.41	2.84×10^{-5}	3.84×10^{-3}
$K^*e\nu_e$	2.15	19.13	0.17	35.07
$\pi e\nu_\mu$	0.237	20.83	3.99×10^{-4}	9.90×10^{-3}
$Ke\nu_e\pi^0$	1.6	18.79	0.19	28.42

Table 4.5: Values of the different efficiencies for each decay channel for the signal decay with the μ in the final state.

Final state	$\mathcal{B}_i$ (%)	ϵ_{GEN} (%)	ϵ_{sel} (%)	$\frac{N_{BKG}}{N_{SIG}}$ (%)
$K\mu\nu_\mu$	3.31	22.44	0.52	100
KK	0.40	22.88	1.02×10^{-3}	0.02
$K\pi\pi\pi^0$	1.43	20	0	0
$K\pi\pi^0$	14.3	19.27	1.77×10^{-3}	1.26
$K3\pi$	8.08	20.00	4.85×10^{-4}	0.20
$K^*\mu\nu_e$	1.86	19.69	0.10	9.69
$\pi\mu\nu_\mu$	0.29	21.29	1.16×10^{-3}	0.02
$K\mu\nu_\mu\pi^0$	1.38	19.42	0.36	24.87
$K^*e\nu_e$	2.15	19.13	1.14×10^{-4}	0.01
$\pi e\nu_\mu$	0.24	20.83	0	0
$Ke\nu_e$	3.55	21.91	2.20×10^{-4}	0.04
$Ke\nu_e\pi^0$	1.6	18.79	1.14×10^{-4}	8.86×10^{-3}

Chapter 5

Conclusions and perspectives

The work presented in this thesis represents a preliminary study for the measurement of the ratio $R_{\mu/e} = \mathcal{B}(D^0 \to K^- \mu^+ \nu_\mu)/\mathcal{B}(D^0 \to K^- e^+ \nu_e)$, using the $D^{*+} \to D^0 \pi^+$ decay chain. The D^{*+} instantly decays into a D^0 and a charged pion. After a flight of few centimeters, the D^0 weakly decays into a kaon, a muon or an electron and the related neutrino, not reconstructible with the LHCb detector. In order to study the value of $R_{\mu/e}$ in all the q^2 region and to calculate the D^{*+} mass using the kinematical information of the daughters of the D^0, a global fit algorithm was implemented in order to estimate the neutrino momentum.

The strategy of the GF algorithm is to write a single function which describes the decay starting from measured quantities, such as the charged particle tracks (K, ℓ, π) and the position of the vertices. In particular, these are the D^0 daughters' momenta $\vec{p}_\nu$, $\vec{p}_\ell$ and $\vec{p}_K$, the coordinates of the pion momentum $\vec{p}_\pi$, the position of the D^0 decay vertex $\vec{x}_{D^0}$ and the third coordinate of the primary vertex z_{PV}. This function includes 5 different kinematical constraints: the D^{*+} decay vertex must corresponds to the primary vertex, which is also the decay vertex of the bachelor π; the displaced vertex of the D^0 decay must be formed by the ℓ and K tracks, and the invariant mass of the D^0, computed using also the ν momentum, must be equal to its known value $1864.83\,\mathrm{MeV}/c^2$ [32]. The statistical approach used is the least chi-square method, and the final parameters are obtained thanks to a nested minimisation.

In this thesis, 2015 Run-2 data and MC samples were used. First the GF was tested on the MC using the MC-"truth" and then on data. For both decay modes (e and μ), the distributions of the invariant mass of the D^{*+} calculated using the output parameters of the GF are compatible with the MC shapes. A study on the different shapes of the D^0 visible mass is obtained for the two deacy modes. The distributions reflect the different reconstruction and identification efficiencies for the e and μ.

In order to reduce the presence of the physical background, due to misidentified final states, a series of PID requirements has been applied and an extended χ^2 fit is performed

on data to extract the signal yields. Only combinatorial background is considered at this stage. However an evaluation of the contamination in the final data sample of the PID-survived decay modes has been carried on, using a dedicated MC data sample.

The work presented in this thesis represents an important contribution of the LHCb-Bologna group to the LHCb working group that carry on the analysis with the aim of performing the final measurement of $R_{\mu/e}$. The higher statistics of the full RUN-2 data sample than the one used in this analysis will permit to extract the signal yields with higher precision. Thanks to the GF algorithm, not only it is possible to extract the signal yields, but also to calculate q^2 and performing a measurement of $R_{\mu/e}$ as function of q^2. This measurement is more sensible to effect of New Physics than the simple measurement of the ratio of the branching frations.

Bibliography

[1] Heavy Flavor Averaging Group, Y. Amhis *et al.*, Eur. Phys. J. **C77** (2017) 895, arXiv:1612.07233, updated results and plots available at http://www.slac.stanford.edu/xorg/hflav/.

[2] H. Georgi and S. L. Glashow, Phys. Rev. Lett. **32** (1974) 438.

[3] S. Weinberg, Phys. Rev. Lett. **19** (1967) 1264.

[4] J. C. Pati and A. Salam, Phys. Rev. D **10** (1974) 275.

[5] F. Englert and R. Brout, Phys. Rev. Lett. **13** (1964) 321.

[6] P. W. Higgs, Phys. Rev. Lett. **13** (1964) 508.

[7] N. Cabibbo, Phys. Rev. Lett. **10** (1963) 531.

[8] M. Kobayashi and T. Maskawa, Prog. Theor. Phys. **49** (1973) 652.

[9] UTfit, http://www.utfit.org/UTfit/. Accessed: 01/02/2018.

[10] S. L. Glashow, J. Iliopoulos, and L. Maiani, Phys. Rev. **D2** (1970) 1285.

[11] C.-N. Yang and R. L. Mills, Physical review **96** (1954), no. 1 191.

[12] S. de Boer and G. Hiller, Phys. Rev. **D93** (2016), no. 7 074001, arXiv:1510.00311.

[13] M. Neubert, Subnucl. Ser. **34** (1997) 98, arXiv:hep-ph/9610266.

[14] HPQCD, J. Koponen *et al.*, arXiv:1305.1462.

[15] S. Fajfer, I. Nisandzic, and U. Rojec, Phys. Rev. **D91** (2015), no. 9 094009, arXiv:1502.07488.

[16] CLEO, J. Y. Ge *et al.*, Phys. Rev. **D79** (2009) 052010, arXiv:0810.3878.

[17] C. Bobeth, G. Hiller, and G. Piranishvili, JHEP **12** (2007) 040, arXiv:0709.4174.

[18] LHCb collaboration, R. Aaij *et al.*, Phys. Rev. Lett. **113** (2014) 151601, arXiv:1406.6482.

[19] Belle, J.-T. Wei *et al.*, Phys. Rev. Lett. **103** (2009) 171801, arXiv:0904.0770.

[20] BaBar, J. P. Lees *et al.*, Phys. Rev. **D86** (2012) 032012, arXiv:1204.3933.

[21] LHCb collaboration, R. Aaij *et al.*, Phys. Rev. Lett. **115** (2015) 111803, arXiv:1506.08614.

[22] S. Fajfer, J. F. Kamenik, and I. Nisandzic, Phys. Rev. **D85** (2012) 094025, arXiv:1203.2654.

[23] BaBar collaboration, J. P. Lees *et al.*, Phys. Rev. Lett. **109** (2012) 101802, arXiv:1205.5442.

[24] LHCb collaboration, R. Aaij *et al.*, arXiv:1708.08856, submitted to Phys. Rev. Lett.

[25] LHCb collaboration, R. Aaij *et al.*, arXiv:1711.02505, submitted to Phys. Rev. D.

[26] BESIII, M. Ablikim *et al.*, arXiv:1802.05492.

[27] LHCb collaboration, R. Aaij *et al.*, JHEP **10** (2016) 030, arXiv:1608.01484.

[28] LHCb collaboration, R. Aaij *et al.*, JHEP **01** (2016) 155, arXiv:1511.08039.

[29] ATLAS, M. Aaboud *et al.*, Eur. Phys. J. **C77** (2017), no. 6 367, arXiv:1612.03016.

[30] L. Evans and P. Bryant, Journal of Instrumentation **3** (2008), no. 08 S08001.

[31] LHCb collaboration, R. Aaij *et al.*, Int. J. Mod. Phys. **A30** (2015) 1530022, arXiv:1412.6352.

[32] Particle Data Group, C. Patrignani *et al.*, Chin. Phys. **C40** (2016), no. 10 100001.

[33] LHCb collaboration, A. A. Alves Jr. *et al.*, JINST **3** (2008) S08005.

[34] LHCb collaboration, CERN-LHCC-2001-011. LHCb-TDR-005.

[35] LHCb collaboration, CERN-LHCC-2013-021. LHCb-TDR-013.

[36] LHCb collaboration, CERN-LHCC-2002-029. LHCb-TDR-008.

[37] LHCb collaboration, CERN-LHCC-2001-024. LHCb-TDR-006.

[38] LHCb collaboration, CERN-LHCC-2000-007. LHCb-TDR-001.

[39] LHCb collaboration, R. Aaij *et al.*, JINST **10** (2015) P02007, arXiv:1408.1251.

[40] LHCb collaboration, R. Aaij *et al.*, Eur. Phys. J. **C74** (2014) 2888, arXiv:1402.4430.

[41] LHCb collaboration, CERN-LHCC-2000-037. LHCb-TDR-003.

[42] LHCb RICH Collaboration, A. Papanestis and C. D'Ambrosio, Tech. Rep. LHCB-PUB-2017-012. CERN-LHCb-PUB-2017-012, CERN, Geneva, Mar, 2017.

[43] LHCb collaboration, CERN-LHCC-2000-036. LHCb-TDR-002.

[44] W. R. Leo, *Techniques for Nuclear and Particle Physics Experiments: A How-to Approach*, Springer, 1994.

[45] H. Fessler *et al.*, Nucl. Instrum. Meth. **A228** (1985) 303.

[46] G. S. Atoyan *et al.*, Nucl. Instrum. Meth. A **320** (1992), no. 1 144 .

[47] the LHCb calorimeter group, I. Machikhiliyan *et al.*, Journal of Physics: Conference Series **293** (2011), no. 1 012052.

[48] P. Perret, LHCb-PROC-2014-017.

[49] LHCb collaboration, CERN-LHCC-2001-010. LHCb-TDR-004.

[50] LHCb collaboration, CERN-LHCC-2003-031. LHCb-TDR-010.

[51] T. Sjöstrand, S. Mrenna, and P. Skands, JHEP **05** (2006) 026, arXiv:hep-ph/0603175.

[52] D. J. Lange, Nucl. Instrum. Meth. **A462** (2001) 152.

[53] Geant4 collaboration, S. Agostinelli *et al.*, Nucl. Instrum. Meth. **A506** (2003) 250.

[54] Geant4 collaboration, J. Allison *et al.*, IEEE Trans. Nucl. Sci. **53** (2006) 270.

[55] D. S. Mitzel and A. Di Canto, Tech. Rep. LHCb-INT-2015-041. CERN-LHCb-INT-2015-041, CERN, Geneva, Nov, 2015.

[56] N. L. Johnson, Biometrika **36** (1949), no. 1-2 149.

Aknowledgments

Vorrei ringraziare tutto il gruppo LHCb di Bologna per la disponibilità dimostrata in ogni momento: dall'insegnarmi la fisica del sapore ad aiutarmi a *debuggare* anche la più antipatica riga di codice. In particolare vorrei ringraziare Federico, il cui aiuto è stato fondamentale per portare al termine il lavoro e Angelo, che è sempre stato disponibile ed entrambi si sono fatti in quattro per aiutarmi nella scrittura della tesi. Ringrazio anche Fabio (*aka* Paglietta), Stefano e Vincenzo per la loro grande disponibilità quotidiana. Grazie anche a Umberto, Antonio e Domenico. Ringrazio inoltre i miei compagni di avventura di tesi a LHCb Serena e Daniele, con cui ho condiviso gioie e ansie.

Questi cinque anni a Bologna mi hanno permesso di crearmi una nuova grande famiglia. Vorrei ringraziare ogni singola persona, ma sicuramente, conoscendomi, mi dimenticherò di qualcuno e mi verrà in mente solo dopo aver caricato il pdf sul sito. In particolare vorrei ringraziare gli *Ansia da prestazione guyz* Marina, Sunny, Octavio, Pit, tutto *il Maru* ed i colleghi magistrali, in particolare Chiara, Giuspe, Marghe e il compagno Riccardo. Grazie anche ad Alessandra, che dal primo giorno di Magistrale, in cui ho pensato: "oh, è appena arrivata non conoscerà nessuno", è diventata una grande amica. Grazie a Caterina, a cui dal 2012 prometto sempre di andare al mare "alle Grotte", ma poi alla fine quel treno non lo prendo mai. Grazie anche alle mie coinquiline, che oltre a sopportarmi quotidianamente, mi danno sempre consigli medici e di vita, soprattutto Myrta. Un grazie doveroso va alla mia prima coinquilina, nonchè prima compagna di banco e curatrice a vita di "cioppi", Giulia. Grazie anche alle amiche di sempre, lontane fisicamente ma vicine: Giorgia, Valentina, Elena, Melissa e soprattutto la Delby. Ringrazio anche tutta la *Big Family* del Circolo, in particolare le *RENGE* Silvia e Ghita e il *RENGO ad honorem*, Mattia.

Infine vorrei ringraziare le persone che mi sono sempre vicine. In primis, vorrei ringraziare i miei parenti, soprattutto i nonni, anche quelli che non ci sono più, che mi hanno insegnato l'importanza dello studio e dell'amore per il proprio lavoro. Un ringraziamento doveroso va sicuramente ai miei genitori, che mi sono sempre stati vicino e mi sostengono ogni giorno. Senza i loro sacrifici non sarei arrivata a questo punto. L'ultimo ringraziamento, ma non per questo meno importante, lo voglio fare a Federico, che mi supporta e mi è vicino ogni giorno.

Grazie mille a tutti.